

# **Self-Assembly and Self-Propulsion of Colloidal Particles Using Shape and**

## **Janus Anisotropy**

by

Onajite Shemi

A dissertation submitted in partial fulfillment  
of the requirements for the degree of  
Doctor of Philosophy  
(Chemical Engineering)  
in the University of Michigan  
2016

Doctoral Committee:

Professor Michael J. Solomon, Chair  
Professor Sharon C. Glotzer  
Professor Joerg Lahann  
Assistant Professor Xiaoming Mao

© Onajite Shemi 2016

## **DEDICATION**

*In memory of LaMont Toliver and Phillip Fitzgerald*

## ACKNOWLEDGEMENTS

The successful completion of my PhD was made possible by many people and I would like to take the time to thank them for their encouragement, mentorship and friendship. Their support contributed to my persevering through the many challenging times during my PhD tenure.

I thank my advisor, Michael Solomon for his guidance and support. I cannot find the words to express how grateful I am to have had him as an advisor. He is a caring, accommodating, and conscientious researcher. He has been my advocate through the years, supporting my ideas and allowing me the freedom to (as he would put it) make things work. From his mentoring style, I gained confidence and independence through trial and error. Then, with every incremental marker of success, introduced new knowledge to the scientific field.

Others that were also instrumental to my training and personal growth are faculty members Omolola Eniola-Adefeso, Mark Burns, Robert Ziff, and Andrew Tadd. Through the sum of my interactions with them, I gained a wealth of scientific knowledge, career advice and words of wisdom. Andrew Tadd also allowed me to share in the joy of teaching undergraduates when I worked for him as a graduate student instructor.

I would also like to thank the community of graduate students that offered me the support in building the necessary skills to be a successful researcher. I would like to thank members of the Solomon group who trained me on synthesis techniques, useful research skills, and communication skills through helpful review of my written work and presentations. Also, as graduate students, we

become accustomed to sharing trade secrets about lab techniques, useful resources, and the best lab equipment for any particular study. My projects were able to progress because of that collaborative exchange of ideas, and for that I thank the graduate students that helped me from Professors Omolola Eniola-Adefeso, Joerg Lahann, Sharon Glozter and Ronald Larson groups.

I would like to thank members of the Chemical Engineering staff. Susan Hamlin, Shelley Fellers, Brian Johnson, Kelly Raickovich, and Laurel Neff for always willing to lend a helping hand. And the staff at the Office of Graduate Education - Kim Elliott, Tiffany Porties, Andria Rose, and Shira Washington. They were a joy to work with when I participated in graduate recruitment and engineering graduate symposium, and I sincerely appreciate the work they do to recruit and retain a diverse body of graduate students at the University of Michigan.

I would like to thank my friends and family, including my future in-laws. I appreciate the phone calls, text messages, meals together, amazing adventures around Michigan and beyond, and for taking the time to uplift my spirits. To my friends who started this journey with me, I am glad we were able to help each other see it through. There is a special bond we share that cannot be duplicated and I hope our paths continue to cross in the future.

And last, but most certainly not least, thank you to my fiancé Gabriel T. Arroyo Jr., for being my partner in everything that I am and everything that I do. I am grateful for our time together as we pursue our personal and professional goals. For the better part of graduate school, you have been the person that I have leaned on the most, and I look forward to us spending the rest of our lives together.

## TABLE OF CONTENTS

<b>DEDICATION</b> .....	<b>ii</b>
<b>ACKNOWLEDGEMENTS</b> .....	<b>iii</b>
<b>LIST OF FIGURES</b> .....	<b>viii</b>
<b>LIST OF TABLES</b> .....	<b>x</b>
<b>ABSTRACT</b> .....	<b>xi</b>

### CHAPTER 1

<b>INTRODUCTION</b> .....	<b>1</b>
1.1 Synthetic methods for Janus particle fabrication .....	2
1.2 Direct visualization method and image analysis.....	2
1.3 Self-assembly methods .....	3
1.4 Janus anisotropy and self-assembly .....	4
1.5 Shape and Janus anisotropy with self-propulsion .....	5
1.6 Shape anisotropy and field-assisted assembly .....	6
1.7 References.....	7

### CHAPTER 2

<b>EFFECT OF SURFACE CHEMISTRY AND METALLIC LAYER THICKNESS ON THE CLUSTERING OF METALLODIELECTRIC JANUS SPHERES</b> .....	<b>11</b>
2.1 Abstract.....	11
2.2 Introduction.....	12
2.3 Methods and Materials.....	14
2.3.1 Janus Particle Synthesis .....	14
2.3.2 Contact Angle Measurements .....	16
2.3.3 Janus Particle Self-Assembly.....	17
2.3.4 Confocal Laser Scanning Microscopy .....	18
2.3.5 Cluster Analysis .....	18
2.4 Results.....	20
2.4.1 Effect of time on cluster probability distribution.....	21
2.4.2 Effect of salt concentration on cluster probability distribution.....	23
2.4.3 Effect of SAM hydrophobicity and chain length on cluster probability distribution.....	26
2.4.4 Effect of gold layer thickness on cluster probability distribution .....	29

2.5	Discussion.....	33
2.6	Conclusion.....	36
2.7	References.....	37
<b>CHAPTER 3</b>		
<b>SELF-PROPULSION OF PLATINUM/POLYSTYRENE JANUS ELLIPSOIDS**</b> .....		<b>40</b>
3.1	Abstract.....	40
3.2	Introduction.....	41
3.3	Materials and Methods.....	43
3.3.1	Janus Ellipsoid Synthesis .....	43
3.3.2	Janus Particle Self-Propulsion .....	45
3.3.3	Confocal Laser Scanning Microscopy .....	45
3.3.4	Image Analysis and Particle Tracking .....	45
3.4	Results.....	47
3.5	Discussion.....	58
3.6	Conclusion .....	61
3.7	References.....	61
<b>CHAPTER 4</b>		
<b>DENSE PACKINGS OF COLLOIDAL OBLATE DISCOIDS</b> .....		<b>64</b>
4.1	Abstract.....	64
4.2	Introduction.....	65
4.3	Materials and Methods.....	66
4.3.1	Janus Discoid Synthesis .....	66
4.3.2	Sample Preparation for Field-Induced Assembly .....	68
4.3.3	Confocal Laser Scanning Microscopy .....	68
4.4	Results.....	69
4.4.1	Kinetics of field-induced assembly.....	69
4.4.2	Packing structure of PS discoids .....	71
4.5	Discussion.....	72
4.6	Conclusion .....	73
4.7	References.....	74
<b>CHAPTER 5</b>		
<b>CONCLUSIONS AND FUTURE WORK</b> .....		<b>77</b>
5.1	Concluding Remarks.....	77
5.2	Future work.....	79
5.3	References.....	80
<b>APPENDIX</b> .....		<b>81</b>

A.1	Contact angle measurements.....	81
A.2	Cluster Analysis.....	83
A.3	Effect of salt concentration on cluster size distribution.....	84
A.4	Effect of SAM hydrophobicity and chain length on cluster size distribution.....	85
A.5	Separation dependent Hamaker coefficient calculations.....	88
A.6	Effective surface coverage using physical vapor deposition.....	89



## LIST OF FIGURES

<b>Figure 2.1</b> Results of Janus particle synthesis.....	16
<b>Figure 2.2</b> CLSM images of assembled Janus particles showing the cluster identification method.....	20
<b>Figure 2.3</b> Clustering kinetics of Janus particles. ....	22
<b>Figure 2.4</b> CLSM images of assembled Janus particles at 1, 2, 2.5, and 3 mM NaCl taken at t = 60 min. ....	24
<b>Figure 2.5</b> Cluster probability distribution at a fixed hemispheric gold thickness (40 nm) and SAM surface chemistry (MOA) as a function of NaCl at t = 60 min.....	25
<b>Figure 2.6</b> CLSM images of assembled Janus particles at 3 mM NaCl.....	27
<b>Figure 2.7</b> Cluster probability distribution at a fixed hemispheric gold thickness (40 nm) and NaCl concentration (3 mM) as a function of SAM surface chemistry. ....	28
<b>Figure 2.8</b> CLSM images of assembled Janus particles with MOA functionality at 3 mM NaCl. ....	30
<b>Figure 2.9</b> Cluster probability distributions at a fixed SAM functionality (MOA) and NaCl concentration (3 mM) as a function gold layer thickness. ....	31
<b>Figure 2.10</b> Separation-dependent nonretarded Hamaker coefficients for various thicknesses of the Au layer on polystyrene (PS), compared to the case of pure PS and pure Au.....	32
<b>Figure 3.1</b> Microscopy images of polystyrene colloidal ellipsoids coated with a 20 nm platinum layer along one-half of the major axis. ....	44
<b>Figure 3.2</b> Images of Janus spheres and ellipsoids in suspension.....	46
<b>Figure 3.3</b> Mobility of spheres in water and 8% (w/v) aqueous hydrogen peroxide solution. ....	48
<b>Figure 3.4</b> CLSM images and centroidal trajectories of Janus ellipsoids in motion in 8% peroxide.....	50
<b>Figure 3.5</b> Illustration of active Janus ellipsoid moving near the coverslip. ....	51
<b>Figure 3.6</b> Schematic of the ellipsoidal particle motion over a time interval and the parameters used to characterize its displacement. ....	52
<b>Figure 3.7</b> Mobility of Janus ellipsoids (AR = $6.7 \pm 0.8$ ) in 8% hydrogen peroxide solution.....	53
<b>Figure 3.8</b> Phoretic mobility of Janus ellipsoids with various aspect ratios in 8% peroxide solution.....	55
<b>Figure 4.1</b> Fabrication technique and micrographs of PS discoids.....	67
<b>Figure 4.2</b> Representative 2D confocal images of PS discoids in 0.1Mm TBAC in DMSO under applied dc voltage. ....	69
<b>Figure 4.3</b> Kinetics of assembly under applied dc voltage and visible light. ....	71
<b>Figure 4.4</b> 2D packing structures of PS colloids in 0.1Mm TBAC in DMSO under applied 2.2V. ....	72
<b>Figure Appendix A.1</b> Wettability of a layer of varied surfaces. ....	82

<b>Figure Appendix A.2</b> CLSM images of assembled Janus particles showing cluster identification method.....	83
<b>Figure Appendix A.3</b> Cluster probability distribution at a fixed hemispheric gold thickness (40 nm) and SAM functionality as a function of NaCl concentration from 1-3 mM. ....	85
<b>Figure Appendix A.4</b> Cluster probability distribution at a fixed hemispheric gold thickness (40 nm) with varied gold functionality. ....	87

## LIST OF TABLES

<b>Table 3-1</b> Characteristics of active motion in ballistic and spinning ellipsoids as a function of aspect ratio in 8% hydrogen peroxide solution.....	69
<b>Table Appendix A.1</b> Contact angles of a monolayer of various surfaces were measured.....	94
<b>Table Appendix A.2</b> Calculated Hamaker coefficients for interfaces included in PS/Au interactions.....	101

## ABSTRACT

Anisotropic colloidal particles can serve as the building block for a variety of complex materials with a range of different functional properties. We demonstrate the properties of anisotropic particles that are complex in shape and surface properties in three different dynamic systems. Shape anisotropy is achieved by increasing particle eccentricity from spheres to ellipsoids and surface anisotropy introduces distinct physical and/or chemical halves to colloidal particles, called Janus particles. In this dissertation, we utilize shape and biphasic properties to generate interesting kinetic and thermodynamic properties of materials. In particular, experimental and theoretical studies allow control to be exercised on self-assembly and self-propulsion on a colloidal scale by our influence on shape and Janus features.

Working with metallodielectric Janus spheres – polystyrene colloids with a hemispheric gold cap – the role of hydrophobicity and gold coating thickness in salt-induced self-assembly is studied. We quantify with both experiment and modeling the distinct surface interactions of these Janus spheres. By varying hydrophobicity, introduced via a covalently bound self-assembled monolayer on the gold surface, from very hydrophilic with 8-mercaptooctanoic acid to highly hydrophobic with 1-octanethiol, we expected differences in preferential binding. However, instead we observe similar clustering properties. We report that increasing the gold layer thickness from 10 nm to 40 nm had a significant effect on the cluster distribution with an abundance of clusters of  $n = 7$  spheres. We theoretically confirm that the observed dominant effect of the metallic layer thickness is a result of van der Waals forces between metallic surfaces with Lifshitz theory; these forces determine the pair potential interactions of the metallodielectric Janus particles. Modeling

these biphasic spheres as multilayered systems predicted the interactions at short and long-range to be up to 60% greater attraction with a 40 nm gold coating than with 10 nm of gold at nanoscale separations.

Metallodielectric colloids can also be produced with ellipsoids and patterned with other metals, thereby introducing shape anisotropy with biphasic interactions. We study the active motion of dilute dispersions of prolate spheroidal polystyrene particles half-coated with platinum along its major axis. The aspect ratio of these ellipsoids range from 2.4 to 6.7. In aqueous suspensions, hydrogen peroxide is catalytically decomposed to water and oxygen by the platinum surface of the Janus particle and the chemical energy is converted into autonomous motion. The induced diffusiophoretic motion of these Janus ellipsoids is determined by direct visualization of their complex trajectories. As the peroxide concentration is increased from 2 to 8 % (w/v), we observe a transition from Brownian to two-dimensional active motion that is resolved by 4 %. The two-dimensional motion of the Janus ellipsoids is subjected to dynamical analysis. We identify two limiting cases from the trajectories – labeled as ballistic and spinning ellipsoids. For ballistic ellipsoids, the mean-squared displacement varies linearly with time on a log-log scale with a significant deviation from unity with a slope of approximately 1.9. The centroidal displacement of spinning ellipsoids grows non-linearly with time and at long lag times there is minimal translational motion. We discuss the physical origins of the observed categories of motion and extract the forces and torques generated from active motion as a function of particle eccentricity. The calculated active force increases with increasing aspect ratio with the 10 times greater activity for ellipsoids with an aspect ratio of 6.7 than 2.4.

Shape anisotropy can also be useful for self-assembly. We examine how oblate spheroids (discoids) densify during field-assisted assembly. We report the application of direct current

electric fields and visible light to suspensions of colloidal discoids to achieve localized dense three-dimensional packings that are both disordered and ordered. Gradients are generated by the electrochemical reactions at the electrode surface to produce a field that drives the electrophoresis of the charged colloids. The application of the dc electric field enables particle assembly and the use of light promotes confinement and improved packing to higher density. The voltage was varied from 1.65 – 2.2 V and a constant laser power of 370 W/m<sup>2</sup>. Experiments were also conducted at a fixed voltage of 1.95 V and a lowered laser intensity of 200 W/m<sup>2</sup>. The two-dimension packing density of the first layer is also reported to be significantly affected by light. The maximum 2D packing density achieved with the dc field alone at 1.95 V was approximately 45%. Of the dc field and visible light combinations tested, the maximum 2D density was approximately 80%. In addition, the first assembled layer was repeated observed to favor hexagonal packing comparable to spheres under stable field conditions.

# CHAPTER 1

## INTRODUCTION

Anisotropic particles on the colloidal scale lend themselves to different morphologies in phoretic and self-assembled systems through increased specificity of dynamical and thermodynamic properties. The range of these colloidal systems – with varied shapes, sizes, and surface properties – are vast and complex, with fabricated colloidal spheres, ellipsoids, disks, or rods be able to modified with an assortment of multi-component and surface properties<sup>1-5</sup>. Controlling the interfacial<sup>6-9</sup> and hydrodynamic forces<sup>10-13</sup> related to these particles can lead to new dynamic and equilibrium properties. These properties can potentially be used to create innovative products and applications including but not limited to medical and technical coatings<sup>14</sup>, and switchable displays for commercial products<sup>15</sup>.

The focus of this dissertation probes the behavior of colloidal particles in different chemical and physical environments as a consequence of their anisotropy. These anisotropic particles vary in shape and material properties. Experiments were conducted with colloidal particles to address the features of Janus anisotropy, shape anisotropy and an intersection of the two. Janus particles are anisotropic particles with physically and/or chemical distinct halves. Shape anisotropy refers to changes in particle geometry, which can in turn lead to complex dynamics, interparticle interactions, and assembly properties. In this work, we systematically controlled particle anisotropy characteristics so as to explore their impact and inform the design of new dynamic systems with anisotropy as a useful building block. We find that the fabricated anisotropic particles generated unusual properties in each of the three different colloidal systems studied. The three

different topics addressed in this dissertation are (i) Janus anisotropy and preferential binding; (ii) Janus and shape anisotropy participation in active motion; and (iii) shape anisotropy influencing phase behavior of dense packing structures.

## **1.1 Synthetic methods for Janus particle fabrication**

There are many sophisticated approaches towards the fabrication of Janus particles. A few methods that have achieved success with producing particles with high specificity include electrohydrodynamic co-jetting<sup>16</sup>, pickering emulsions<sup>3,17</sup>, and physical vapor deposition (PVD)<sup>18</sup>. Of these methods, PVD is utilized in the Janus colloids fabricated for the different systems in this dissertation. It is favored because of its simplicity in generating nanoscale coatings of metals such as iron<sup>10</sup>, platinum<sup>11</sup>, and gold<sup>19</sup>, with gold adhering to the polymeric surface if a thin passivating layer such as titanium<sup>19</sup> or chromium<sup>12</sup> is first applied. When applied to monolayers of polymeric spheres, PVD generates a metallodielectric functionality that is appreciated in inducing large particle-particle and particle-solvent interaction differences between the metallic and dielectric hemispheres of the Janus colloids. In Chapter 2, we fabricate polystyrene spheres coated on one hemisphere with gold and in Chapter 3, we fabricate polystyrene ellipsoids half-coated along the major axis with platinum.

## **1.2 Direct visualization method and image analysis**

We use confocal laser scanning microscopy to image the dynamics of the three colloidal systems presented in this dissertation. It provides high resolution real-time images of the biphasic colloidal particles and provides an accurate representation of the different fabricated shapes. This method of studying the structure and dynamics of different suspensions utilizes light scattering



and emission collection at an objective plane within my sample, ranging several microns above the coverslip. The depth of analysis is further improved using organic solvents, refractive index and density matched suspensions, and monodispersed colloids<sup>20</sup>. In Chapters 2 and 3, with systems involving Janus anisotropy using metals, gold and platinum, the particles sediment upon equilibration and all interactions that occurred were captured within the field of view afforded for aqueous systems. The lateral and perpendicular optical resolutions enable the characterization of the different hemispheres of the Janus colloid. Using a dual channel frequency, at an excitation of 488 laser, the reflection of the metal hemisphere is observed and the emitted light from the fluorescent latex hemisphere are visualized with the 561 nm laser over the range 570 to 620 nm. In Chapter 4, we visualize the rapid deposition of colloidal discoids in non-aqueous suspensions and ascertain its orientation in real time. We also utilize scanning electron microscopy and transmission electron microscopy to assess the topography and physical characteristics of the anisotropic particles.

### **1.3 Self-assembly methods**

The mobility of particles on the nano- and microscale can be motivated by various methods<sup>11,21-25</sup>. Many of these methods also aim to achieve self-assembly of interesting ordered and disordered structures in 2D and 3D. By applying external fields and inducing gradients via chemical reactants<sup>25,26</sup>, gravitational fields<sup>27,28</sup>, electric fields<sup>12,13,22,29,30</sup>, magnetic fields<sup>31,32</sup> and visible light<sup>33</sup>, we attain highly reconfigurable assemblies. In Chapters 2 and 4, we demonstrate assemblies of anisotropic colloids using external stimulants. We report clustering of PS-Au Janus spheres – regulated with the addition of salt – from isolating its biphasic anisotropy. To achieve

dense packing of PS oblate discoids, we perform a combinatory process of applied electric field and visible light.

## **1.4 Janus anisotropy and self-assembly**

The work described in Chapter 2 addresses the subject of biphasic surface anisotropy with Janus spheres, and the governing inter-particle interactions as a new system equilibrium is reached. There are kinetic and thermodynamic properties that influence particle motion leading to enthalpically and entropically favored assembly<sup>1,19,25</sup>. In advanced materials and sensors research, there are bicolored and metallic Janus spheres that self-assemble to show one face in response to the presence of an electric field<sup>34</sup>. New surfactants can be synthesized utilizing the anisotropy of particles to decrease the surface tension at the interface of opposing fluids<sup>35</sup>. In this system, we explore Janus spheres with a conductive metallic hemisphere and polymer latex hemisphere. Utilizing both metallic and dielectric properties offers versatility in the assembly of complex cluster geometries<sup>19,25</sup> and open crystal lattices<sup>26</sup>.

Colloidal dispersions of polystyrene (PS) spheres coated with gold (Au) can be chemically induced to self-assemble into ordered clusters. The Janus complexity draws from carboxylate charge-stabilized PS, the Au coating, and functionalizing the Au with a hydrophilic or hydrophobic self-assembled monolayer (SAM). Under varied salt conditions, there is non-covalent attractive binding of the Au hemispheres observed in competition with repulsive interactions of the negatively charged PS hemispheres. Controlling the Debye length, the length at which electrostatic interactions are screened due to free charges surrounding a surface, by varying salt concentration results in various cluster densities. Attempts have been made to quantitatively explain and predict salt concentrations at which clusters are observed with pair potential calculations and molecular

dynamics simulation<sup>19,25</sup>. However, here the explicit driving force for assembly is discussed in consideration of Au thickness, and SAM hydrophobicity for cluster formation and stability.

## 1.5 Shape and Janus anisotropy with self-propulsion

The work described in Chapter 3 explores metallodielectric colloids that have been elongated from spheres to prolate ellipsoids by means of mechanical deformation. The increased shape anisotropy and surface curvature in ellipsoids relative to spheres is instrumental to their performance in applications such as improved near-wall particle flow<sup>36</sup> and adhesion<sup>37</sup>, the generation of highly packed ordered structures for optical devices<sup>38</sup>, and use in consumer products<sup>39</sup>. Research has shown Janus spheres exhibit chemically induced self-propulsion at the surface of transition metals such as platinum (Pt)<sup>11,24,40-42</sup>. Using aqueous hydrogen peroxide as a fuel, a catalytic reaction occurs on the Pt coating on Janus and other types of anisotropic particles; this chemical transformation of energy causes the particles to move by means of self-diffusiophoresis. The directed propulsion can vary from seconds<sup>11,21,23,41</sup> to hours<sup>43</sup>. Here we report new directions of mobility and increased active mobility using PS-Pt ellipsoids. Past work with active motion of anisotropic colloids has been limited to the shapes of spheres<sup>11</sup>, clusters of spheres<sup>24,44</sup>, rods<sup>23</sup>, and miscellaneous shapes<sup>43,45</sup>. The first work to show active motion of rods were in fact in a bimetallic system; in this case the Janus configuration was of combined cylindrical segments of gold and platinum to create one nanorod<sup>23</sup>. Here the configuration studied is latex prolate ellipsoids with a Pt coating along the major axis. The bimetallic rods and rod-like prolate ellipsoids differ according to eccentricity along the major axis and the Janus orientation.

Working with ellipsoids in place of spheres could reveal additional regimes of active dynamics. We find that colloidal dispersions of PS spheres coated with Pt can be chemically

induced to self-propel ballistically and spin rapidly. We study the diffusive properties as a consequence of the systematic variation of hydrogen peroxide concentration and particle aspect ratio (and thereby surface area), through particle tracking. The anisotropic geometry of the ellipsoids generates propulsive motion perpendicular to the major axis of the ellipsoid. We report that the dynamic motion of these Janus ellipsoids leads to interesting active trajectories, with varying contributions of translational and rotational displacement observed.

## **1.6 Shape anisotropy and field-assisted assembly**

The work described in Chapter 4 explores the kinetics and packing of colloidal discoids. In the natural world, the building blocks that yield intriguing biophotonic structures are often anisotropic in shape and interactions. The phase behavior of the biological constituents result in diffracted light of wavelengths in the visible range, creating impressive structural colors<sup>46</sup>. Long-range ordered arrays of particles, that are predominantly spheres, can be used to create photonic crystals<sup>47</sup>. However, anisotropic building blocks are predicted to yield ordered assemblies that are more densely packed than spheres with potentially unique wavelength-diffracting patterns. Working with discoids is proposed as pathway to achieve structural color in artificial materials. Some of the challenges in achieving such high density packings of anisotropic particles can be bypassed by applying external fields including gravitational fields<sup>27,28</sup>, electric fields<sup>12,13,22,29,30</sup>, magnetic fields<sup>31,32</sup> and visible light<sup>33</sup>. We report the assembly kinetics and steady state packing density of discoids assembled by direct current (dc) electric field and visible light.

Colloidal dispersions of PS discoids in a non-aqueous solution of dimethyl sulfoxide (DMSO) were driven to assemble into closely packed structures by means of dc electric field and visible light. The shape anisotropy explored is distinct the types of anisotropic colloids studies by

others<sup>21,48</sup>. Under particular dc voltage and visible light conditions, rapid assembly of the PS discoids is observed. Controlling the dc voltage manipulates the ion gradients generated by the electrochemical reactions at the electrode surface; this manipulation results in the electrophoresis of the charged colloids, generating different disk packing densities. The electrophoretic deposition, packing density, and resulting structures is discussed with respect to the current density generated by applied voltage and visible light intensity.

## 1.7 References

1. Glotzer, S. C.; Solomon, M. J. Anisotropy of Building Blocks and Their Assembly into Complex Structures. *Nat. Mater.* **2007**, *6* (8), 557–562.
2. Walther, A.; Mu, A. H. E. Janus Particles. *Soft Matter* **2008**, *4*, 663–668.
3. Jiang, S.; Chen, Q.; Tripathy, M.; Luijten, E.; Schweizer, K. S.; Granick, S. Janus Particle Synthesis and Assembly. *Adv. Mater.* **2010**, *22* (10), 1060–1071.
4. Sacanna, S.; Pine, D. J. Shape-Anisotropic Colloids: Building Blocks for Complex Assemblies. *Curr. Opin. Colloid Interface Sci.* **2011**, *16* (2), 96–105.
5. Lee, K. J.; Yoon, J.; Lahann, J. Recent Advances with Anisotropic Particles. *Curr. Opin. Colloid Interface Sci.* **2011**, *16* (3), 195–202.
6. Parsecian, V. A.; Ninham, B. W. Van Der Waals Forces in Many-Layered Structures : Generalizations of the Lifshitz Result for Two Semi-Infinite Media. *J. Theor. Biol.* **1973**, *38*, 101–109.
7. Ederth, T. Computation of Lifshitz - van Der Waals Forces between Alkylthiol Monolayers on Gold Films. *Langmuir* **2001**, *17* (11), 3329–3340.
8. Anderson, J. L. Colloid Transport by Interfacial Forces. *Annu. Rev. Fluid Mech.* **1989**, *21* (1), 61–99.
9. Israelachvili, J. N. *Intermolecular and Surface Forces*; **2011**.
10. Smoukov, S. K.; Gangwal, S.; Marquez, M.; Velev, O. D. Reconfigurable Responsive Structures Assembled from Magnetic Janus Particles. *Soft Matter* **2009**, *5* (6), 1285.
11. Howse, J.; Jones, R.; Ryan, A.; Gough, T.; Vafabakhsh, R.; Golestanian, R. Self-Motile Colloidal Particles: From Directed Propulsion to Random Walk. *Phys. Rev. Lett.* **2007**, *99* (4), 48102.

12. Gangwal, S.; Cayre, O. J.; Velev, O. D. Dielectrophoretic Assembly of Metallodielectric Janus Particles in AC Electric Fields. *Langmuir* **2008**, *24* (23), 13312–13320.
13. Shah, A. a; Ganesan, M.; Jocz, J.; Solomon, M. J. Direct Current Electric Field Assembly of Colloidal Crystals Displaying Reversible Structural Color. *ACS Nano* **2014**, *8* (8), 8095–8103.
14. Janssen, M. .; van Leeuwen, M. B. .; Scholtmeijer, K.; van Kooten, T. .; Dijkhuizen, L.; Wösten, H. A. . Coating with Genetic Engineered Hydrophobin Promotes Growth of Fibroblasts on a Hydrophobic Solid. *Biomaterials* **2002**, *23* (24), 4847–4854.
15. Velev, O. D.; Gupta, S. Materials Fabricated by Micro- and Nanoparticle Assembly - The Challenging Path from Science to Engineering. *Adv. Mater.* **2009**, *21* (19), 1897–1905.
16. Bhaskar, S.; Lahann, J. Microstructured Materials Based on Multicompartmental Fibers. *J. Am. Chem. Soc.* **2009**, *131* (19), 6650–6651.
17. Hong, L. Simple Method to Produce Janus Colloidal Particles in Large Quantity. *Langmuir* **2006**, *22* (12), 9495–9499.
18. Gangwal, S.; Pawar, A.; Kretzschmar, I.; Velev, O. D. Programmed Assembly of Metallodielectric Patchy Particles in External AC Electric Fields. *Soft Matter* **2010**, *6* (7), 1413.
19. Hong, L.; Cacciuto, A.; Luijten, E.; Granick, S. Clusters of Amphiphilic Colloidal Spheres. *Langmuir* **2008**, *24* (3), 621–625.
20. Solomon, M. J.; Kogan, M. Confocal Optical Microscopy. *Encyclopedia of Condensed Matter Physics*; Elsevier, 2005; Vol. 1, pp 229–235.
21. Erbe, a; Zientara, M.; Baraban, L.; Kreidler, C.; Leiderer, P. Various Driving Mechanisms for Generating Motion of Colloidal Particles. *J. Phys. Condens. Matter* **2008**, *20*, 404215.
22. Gangwal, S.; Cayre, O. J.; Bazant, M. Z.; Velev, O. D. Induced-Charge Electrophoresis of Metallodielectric Particles. *Phys. Rev. Lett.* **2008**, *100* (5), 1–4.
23. Paxton, W. F.; Kistler, K. C.; Olmeda, C. C.; Sen, A.; St. Angelo, S. K.; Cao, Y.; Mallouk, T. E.; Lammert, P. E.; Crespi, V. H. Catalytic Nanomotors: Autonomous Movement of Striped Nanorods. *J. Am. Chem. Soc.* **2004**, *126* (41), 13424–13431.
24. Gao, W.; Pei, A.; Feng, X.; Hennessy, C.; Wang, J. Organized Self-Assembly of Janus Micromotors with Hydrophobic Hemispheres. *J. Am. Chem. Soc.* **2013**, *135* (3), 998–1001.
25. Chen, Q.; Whitmer, J. K.; Jiang, S.; Bae, S. C.; Luijten, E.; Granick, S. Supracolloidal Reaction Kinetics of Janus Spheres. *Science* **2011**, *331* (6014), 199–202.

26. Chen, Q.; Bae, S. C.; Granick, S. Directed Self-Assembly of a Colloidal Kagome Lattice. *Nature* **2011**, *469* (7330), 381–384.
27. Savenko, S. V.; Dijkstra, M. Sedimentation and Multiphase Equilibria in Suspensions of Colloidal Hard Rods. *Phys. Rev. E* **2004**, *70*.
28. Mukhija, D.; Solomon, M. J. Nematic Order in Suspensions of Colloidal Rods by Application of a Centrifugal Field. *Soft Matter* **2010**, *7*, 540–545.
29. Trau, M.; Saville, D. A.; Aksay, A. Field-Induced Layering of Colloidal Crystals. *Sci. New Ser.* **1996**, *272* (5262), 706–709.
30. Rogach, a L.; Kotov, N. a; Koktysh, D. S.; Ostrander, J. W.; Ragoisha, G. a. Electrophoretic Deposition of Latex-Based 3D Colloidal Photonic Crystals : A Technique for Rapid Production of High-Quality Opals. *Chem. Mater.* **2000**, No. 16, 2721–2726.
31. Ahniyaz, A.; Sakamoto, Y.; Bergström, L. Magnetic Field-Induced Assembly of Oriented Superlattices from Maghemite Nanocubes. *Proc. Natl. Acad. Sci. U. S. A.* **2007**, *104* (45), 17570–17574.
32. Ding, T.; Song, K.; Clays, K.; Tung, C. H. Fabrication of 3D Photonic Crystals of Ellipsoids: Convective Self-Assembly in Magnetic Field. *Adv. Mater.* **2009**, *21* (19), 1936–1940.
33. Kim, Y.; Shah, A. A.; Solomon, M. J. Spatially and Temporally Reconfigurable Assembly of Colloidal Crystals. *Nat. Commun.* **2014**, *5*, 1–8.
34. Nisisako, T.; Torii, T.; Takahashi, T.; Takizawa, Y. Synthesis of Monodisperse Bicolored Janus Particles with Electrical Anisotropy Using a Microfluidic Co-Flow System. *Adv. Mater.* **2006**, *18* (9), 1152–1156.
35. Glaser, N.; Adams, D. J.; Böker, A.; Krausch, G. Janus Particles at Liquid-Liquid Interfaces. *Langmuir* **2006**, *22* (12), 5227–5229.
36. Gavze, E.; Shapiro, M. Particles in a Shear Flow near a Solid Wall: Effect of Nonsphericity on Forces and Velocities. *Int. J. Multiph. Flow* **1997**, *23* (1), 155–182.
37. Lee, S. Y.; Ferrari, M.; Decuzzi, P. Design of Bio-Mimetic Particles with Enhanced Vascular Interaction. *J. Biomech.* **2009**, *42* (12), 1885–1890.
38. Kim, S.-H.; Lee, S. Y.; Yang, S.-M.; Yi, G.-R. Self-Assembled Colloidal Structures for Photonics. *NPG Asia Mater.* **2011**, *3* (1), 25–33.
39. Donev, A.; Cisse, I.; Sachs, D.; Variano, E. A.; Frank, H.; Connelly, R.; Torquato, S.; Chaikin, P. M. Improving the Density of Jammed Disordered Packings Using Ellipsoids. *Science* (80). **2004**, *303* (5660), 990–993.
40. Ebbens, S.; Gregory, D. A.; Dunderdale, G.; Howse, J. R.; Ibrahim, Y.; Liverpool, T. B.;

- Golestanian, R. Electrokinetic Effects in Catalytic Platinum-Insulator Janus Swimmers. *EPL (Europhysics Lett.)* **2014**, *106* (5), 58003.
41. Ke, H.; Ye, S.; Carroll, R. L.; Showalter, K. Motion Analysis of Self-Propelled Silica Particles in Hydrogen Peroxide Solutions. *J. Phys. Chem. A* **2010**, *114* (17), 5462–5467.
  42. Ebbens, S.; Howse, J. R. Direct Observation of the Motion Direction for Spherical Catalytic Swimmers. *Langmuir* **2011**, *5* (1977), 6916–6923.
  43. Ismagilov, R.; Schwartz, A.; Bowden, N.; Whitesides, G. Autonomous Movement and Self-Assembly. *Angew.* **2002**, *114* (4), 674–676.
  44. Ebbens, S.; Jones, R. A. L.; Ryan, A. J.; Golestanian, R.; Howse, J. R. Self-Assembled Autonomous Runners and Tumblers. *Phys. Rev. E - Stat. Nonlinear, Soft Matter Phys.* **2010**, *82* (1), 6–9.
  45. Gao, W.; Sattayasamitsathit, S.; Orozco, J.; Wang, J. Highly Efficient Catalytic Microengines: Template Electrosynthesis of Polyaniline/platinum Microtubes. *J. Am. Chem. Soc.* **2011**, *133* (31), 11862–11864.
  46. Dufresne, E. R.; Noh, H.; Saranathan, V.; Mochrie, S. G. J.; Cao, H.; Prum, R. O. Self-Assembly of Amorphous Biophotonic Nanostructures by Phase Separation. *Soft Matter* **2009**, *5* (9), 1792.
  47. Colvin, V. L. From Opals to Optics: Colloidal Photonic Crystals. *MRS Bull.* **2001**, *26* (8), 637–641.
  48. Whitesides, G. M.; Boncheva, M. Beyond Molecules: Self-Assembly of Mesoscopic and Macroscopic Components. *Proc. Natl. Acad. Sci. U. S. A.* **2002**, *99* (8), 4769–4774.



## CHAPTER 2

### EFFECT OF SURFACE CHEMISTRY AND METALLIC LAYER THICKNESS ON THE CLUSTERING OF METALLODIELECTRIC JANUS SPHERES

#### 2.1 Abstract

The non-covalent binding of the gold hemispheres of polystyrene/gold colloidal Janus spheres in aqueous solution was found to depend more significantly on the deposition thickness of the particle's gold layer than the chemistry of a covalently affixed self-assembled monolayer on the gold. By means of two-channel confocal laser scanning microscopy, salt-induced clustering was observed and quantified for Janus particles with gold hemispheres functionalized with a thiol self-assembled monolayer that varied in hydrophobicity and chain length. The thickness of the gold layer on the Janus particles was also varied from 10 nm to 40 nm. The measured cluster distributions were strongly salt dependent, with clustering absent at 1 mM salt condition but present at concentrations in the range of 2 – 3 mM salt. For Janus spheres with a 40 nm thick gold hemisphere, the effects of both thiol monolayer hydrophobicity and chain length were modest. Varying the gold layer thickness between 10 nm to 40 nm, however, had a significant effect on the cluster distribution; the most abundant cluster size shifted from one to seven particles as gold layer thickness increased from 10 to 40 nm. Thus, the gold layer thickness had a greater effect than

---

\*The text in this chapter was originally published in [O. Shemi & M.J. Solomon, *Langmuir*, **2014**, 30, 15408-15415].

either self-assembled monolayer hydrophobicity or chain length on the self-assembly of metallodielectric Janus particles into clusters. The dominant effect of the metallic layer thickness suggests that van der Waals forces between metallic surfaces are more important than hydrophobic interactions in determining the pair potential interactions of metallodielectric Janus particles.

## 2.2 Introduction

Janus colloids – particles with distinct physical and/or chemical halves – have the potential to behave differently than isotropic particles because of the dissimilar potential interactions between the two halves of the particle.<sup>1</sup> The polymeric, chemical and/or metallic anisotropy of Janus spheres can be introduced by techniques such as microfluidics<sup>2</sup>, co-jetting<sup>3</sup>, Pickering emulsions<sup>4</sup>, and physical vapor deposition (PVD)<sup>5</sup>. Among these methods, PVD is very promising because of its simplicity and because it generates nanoscale coatings of metals such as iron<sup>6</sup>, platinum<sup>7</sup>, and gold<sup>8</sup>, with gold adhering to the polymeric surface if a thin passivating layer such as titanium<sup>8</sup> or chromium<sup>9</sup> is first applied. When applied to monolayers of polymeric spheres, PVD generates a metallodielectric functionality that is valuable because it induces large interaction differences between the metallic and dielectric hemispheres of the Janus colloids.

Consequently, Janus spheres of polystyrene and gold are of particular interest for self-assembly because of their anisotropic character and simple fabrication. Addition of salt to aqueous suspensions of these particles induces their self-assembly into clusters, as well as large-scale structures such as Bernal spirals<sup>8,10</sup>. These particles therefore extend the scope for fundamental exploration of clustering and anisotropic colloidal self-assembly<sup>11</sup>. The self-assembled structures themselves have potential applications in sensing, in micro- and nanofabrication, and in

microelectronics<sup>12</sup>. For example, polystyrene/gold Janus particles can assemble into a 2D crystal in the presence of an AC electric field<sup>9</sup> and have been investigated as a multifunctional sensor with the ability to specifically target breast cancer cells<sup>13</sup>.

The hydrophobic effect has been described as the origin of the preferential binding of the metallic halves of gold-latex Janus particles<sup>8,14</sup>. This effect is thought to arise as a consequence of the thiol species that are commonly used to functionalize the gold surface. Specifically, a hydrophobic thiol self-assembled monolayer (SAM) affects the structure of the near-surface solvent. The non-polar constituents of these thiols generate a potential of mean force between the two gold surfaces by inducing an entropy change of the solvent. In addition, the metallic hemispheres of Janus particle interact through screened electrostatic repulsion and van der Waals (vdW) attractions. These electrostatic and dispersion interactions are a function of the dielectric properties of the latex and the solvent, the geometry and the orientation of the particles, and the thickness of the metal layer<sup>6,15,16</sup>. The effect of thickness arises because a layered surface of material generates bulk-like surface forces only as the thickness of the coating is increased beyond a distance that varies with material, but has been found to be in the range of 40 to 100 nm<sup>17</sup>.

Although there is general agreement of the role of hydrophobic, electrostatic, and van der Waals forces in the pair interaction between the metallic hemispheres of Janus particles, the specific degree to which the particular thiol species contribute to this pairwise interaction is unclear. Theory and simulations have described their influence<sup>8,18</sup>, and interfacial experiments have quantified the attractive and repulsive interactions introduced with thiol-functionalized gold-latex particles<sup>19</sup>. However, these studies leave open the central question of whether or not the observed attraction between the gold faces of metallodielectric Janus particles is predominantly controlled by hydrophobic interactions or by van der Waals interactions. Therefore, the aim of this

study is to evaluate the relative contribution of these effects to Janus colloidal self-assembly and clustering by parametrically varying the strength of each effect within a single study.

To probe the relative effect of hydrophobic and van der Waals forces to the Janus particle interaction, in this paper we systematically vary these forces by changing the thickness of the deposited gold layer and the hydrophobicity – as indicated by the contact angle – of the thiol self-assembled monolayer that is bound to the gold hemisphere. We understand the effect of varying these physical parameters on Janus particle self-assembly by measuring the change they yield in the size distribution of ordered clusters produced by the specific Au-to-Au binding.

Identification of the relative contribution of these interactions to the Janus particle binding will improve: (i) the scope for modeling the pair interaction potential of Janus particles; (ii) the understanding of how the strength and range of the Janus anisotropic interactions may be varied; and (iii) the efforts to quantitatively compare simulations and experiments of the phase behavior, clustering, and self-assembly of Janus particles.

## **2.3 Methods and Materials**

### **2.3.1 Janus Particle Synthesis**

Gold-coated polystyrene particles (PS-Au) were fabricated by physical vapor deposition (PVD) as adapted from literature methods<sup>5,8,9</sup>. Briefly, 100 mL of a 2.0 vol % solution of  $1.0 \pm 0.03 \mu\text{m}$  carboxylate-modified polystyrene spheres (PS) (F8821, Life Technologies) is solvent-exchanged with 400  $\mu\text{L}$  of 200 proof ethanol (E7023, Sigma-Aldrich) using centrifugation. This suspension of spheres is spin-coated onto a glass microscope slide (glass coverslip, 35 mm x 50 mm x 0.13 mm, Fisher Scientific) using a Laurell spin coater at 300 rpm for 20 s, then 3000 rpm

for 20 s, to create a single particle monolayer. We preclean the glass microscope slides by soaking them in a 0.1 N potassium hydroxide solution (319325, Sigma-Aldrich) for 15 min. The zeta-potential of the uncoated polystyrene particles was measured to be  $-69 \pm 1$  mV in DI water,  $-89 \pm 1$  mV in 1 mM NaCl,  $-83 \pm 2$  mV in 2 mM NaCl,  $-78 \pm 4$  mV in 2.5 mM NaCl, and  $-71 \pm 1$  mV in 3 mM NaCl (Nano-ZS, Malvern Instruments).

Thin layers of titanium (2.5 nm thickness) and gold (10, 20, or 40 nm) are sequentially deposited on the particle monolayers via PVD using an e-beam evaporator (Denton Vacuum). The evaporator deposits the metals on just one hemisphere of the spherical particles to create Janus spheres. The slides with attached Janus spheres are submerged in 2 mM thiol solutions to produce the self-assembled monolayer (SAM) that is covalently bound to the gold hemisphere of the particles<sup>20,21</sup>. The thiol solutions are prepared by dilution of 1-octanethiol (OT) (471836, Sigma-Aldrich), 8-mercaptooctanoic acid (MOA, 675075, Sigma-Aldrich), or 16-mercaptohexadecanoic acid (MHDA, 448303, Sigma-Aldrich) in 200 proof ethanol (E7023, Sigma-Aldrich). Janus particles with varying gold layer thickness, as produced by the synthesis and then imaged by scanning electron microscopy (Philips XL-30), are reported in Figure 2.1a-c. Figure 2.1a-c shows that the physical deposition of the gold produces a uniform, contiguous layer at each of the conditions of 10 nm, 20 nm, and 40 nm thickness, respectively.

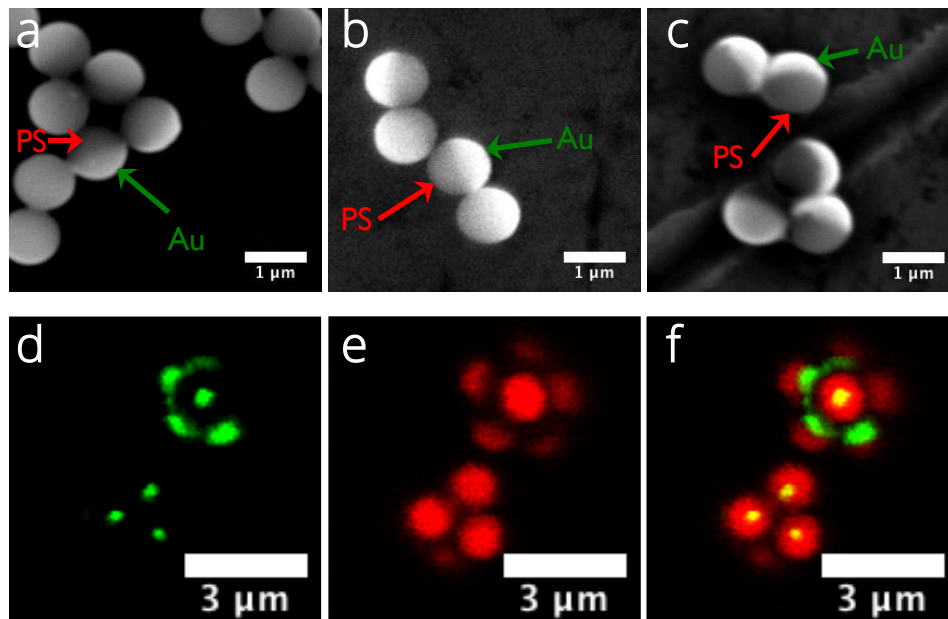


**Figure 2.1 Results of Janus particle synthesis.**

(a–c) SEM images of synthesized particles using  $1.0 \pm 0.03 \mu\text{m}$  measured carboxylate-modified polystyrene spheres. The brighter hemisphere in panels a–c shows the Au coating with thicknesses of (a) 10, (b) 20, and (c) 40 nm. (d–f) Two-channel CLSM images of Janus particles assembled into clusters. (d) Reflection mode imaging (488 nm) shows the Au hemisphere. (e) Fluorescence mode imaging (561 nm excitation) shows the fluorescent PS section of the Janus particle. (f) An overlay of the two images identifies the Janus functionality, the orientation of the Au hemisphere, and the Au-to-Au binding. This figure was originally published in [Shemi, O.; Solomon, M. J. *Langmuir* **2014**, *30*, 15408–15415].

### 2.3.2 Contact Angle Measurements

We evaluate the hydrophobicity of the gold hemispheres by measuring the contact angle of a water droplet on a monolayer of the synthesized Janus particles. This was done after the thiol functionalization step of the synthesis but before removing the monolayer of Janus spheres from the glass microscope slide. The equilibrium contact angle,  $\theta$ , of Janus spheres functionalized with OT, MOA, MHDA, and a control of no thiol functionalization was compared to that of carboxylate-modified polystyrene via measurements of water droplet images (shown in Figure Appendix A.1, with results organized in Table Appendix A.1). The equilibrium contact angle

provides a quantitative characterization of the wettability of the Janus spheres compared to bare polystyrene.

The measured contact angles for the different surfaces vary from  $\theta = 19^\circ$  to  $\theta = 115^\circ$  per Table Appendix A.1. The high contact angle for OT ( $\theta = 115^\circ$ ) is consistent with the hydrophobic side chains and end group of this species. MOA ( $\theta = 26^\circ$ ) and MHDA ( $\theta = 50^\circ$ ) are more hydrophilic than OT due to their acidic functional groups. In addition, hydrophobicity increases from MOA to MHDA consistent with the longer saturated aliphatic region of the latter's chemical structure. To determine if the micron-scale periodicity of the monolayer of Janus microspheres affected the measurement of the contact angle, a second set of contact angle measurements was conducted for planar layers of 40 nm gold that had been thiol-functionalized (shown also in Figure Appendix A.1). The wettability of each modified Au surface in this case is consistent with the first set of measurements, as reported in Table Appendix A.1. That is, the homologous variation of contact angle of the different SAMs from high to low as OT, MDHA, MOA is conserved regardless of whether the Janus spheres or planar layers are tested. This congruence indicates that the micron scale roughness of the deposited Janus spheres does not impact our qualitative assignment of the degree of wettability/hydrophobicity of these thiol-modified gold surfaces.

### **2.3.3 Janus Particle Self-Assembly**

Experiments are conducted in Lab-Tek™ II 8-well chambered cover glass (155409, Fisher Scientific). The wells are first cleaned and activated in a photosensitized oxidative chamber (Jelight UVO Cleaner) for 20 min before a 150  $\mu\text{l}$  dispersion of Janus spheres of volume fraction  $1.0 \times 10^{-5}$  is transferred to a well. The activation prevents Janus particle adsorption to the glass surface. An equal volume of NaCl solution is then added to give final experimental concentrations

of 1 mM, 2 mM, 2.5 mM or 3 mM; the two solutions are mixed with a pipette tip. The system is observed by confocal microscopy (CLSM, Leica TCS SP2 or Nikon A1R) just prior to the addition of the salt solution to confirm initial stability of the Janus particles. The kinetic study to establish the time to system equilibrium, mediating concerns of sedimentation due to particle/solvent density mismatch, and particle and cluster exploration, observed clusters at fixed intervals after the salt solution is added, as described in the Results. All other cluster probability distribution studies were evaluated 60 min after the addition of NaCl, as also justified in the Results.

### **2.3.4 Confocal Laser Scanning Microscopy**

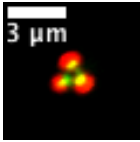
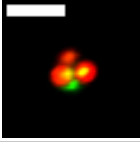
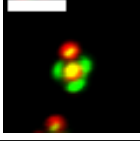
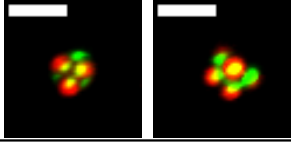
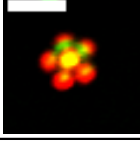
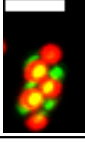
For each experiment, three independent CLSM image volumes were acquired using a Nikon A1R CLSM instrument with a 100x, 1.4NA, oil immersion objective lens. The gold portion of the Janus particle is predominantly imaged in reflection mode, as it is more reflective than the polystyrene, at 488nm (Figure 2.1d) and the fluorescent polystyrene is imaged in fluorescence mode by excitation with the 561 nm laser (Figure 2.1e). The fluorescence emission is collected over the range 570 to 620 nm. The combined two-color image, which shows the orientation of the Janus hemispheres in the cluster, is shown in Figure 2.1f. Images volumes were comprised of a stack of images of dimension 512 pixel x 128 pixel. The number of slices varied from 80 to 100 to accommodate the variable effect of cluster sedimentation. Scanning is terminated at the coverslip, the time to capture a typical image volume is ~ 15 seconds, and the voxel size is approximately 124 x 124 x 100 nm<sup>3</sup>.

### **2.3.5 Cluster Analysis**

The number of particles in each cluster was counted by applying the known configuration of a particular cluster size of isotropic and Janus spheres, as available in the literature.<sup>14,22</sup> In the



few cases in which all the spheres in a cluster could not be clearly observed in the image volumes, the cluster number was inferred with additional reference to the configuration of particles in the cluster. As discussed by Granick and co-workers,<sup>8,14</sup> and also shown in Figure 2.2, clusters of different size adopt particle configurations that are distinguishable from each other. Within the scope of this study of 1 – 3 mM NaCl, the various cluster sizes observed were of distinguishable geometries. In addition to linear dimers ( $n = 2$ ) of hemispheric gold binding, configurations ranging from triangles ( $n = 3$ ) to pentagonal dipyrramids ( $n = 7$ ) were observed. The presence of larger clusters ( $n = 8+$ ) was minimal and exhibited various configurations but was still accounted for. We determine the clustering probability of a Janus sphere by calculating the fraction,  $x_n$ , of the number of Janus particles in the counted clusters of size  $n$ , called  $C_n$ , out of the total number of available Janus particles,  $N_{total}$ , such that  $x_n = nC_n / \sum_n nC_n = nC_n / N_{total}$ . We conducted three independent trials for each experimental condition and the number of clusters analyzed for each curve varies between 90 and 250 and the total number of Janus colloids incorporated into these clusters varies from 150 to 400. The error bars we report are the deviations based on the three trials.

N	Cluster	Geometry
3		Triangle
4		Tetrahedron
5		Triangular dipyramid
6		Octahedron (left) & Capped trigonal bipyramid (right)
7		Pentagonal dipyramid
8+		Varies

**Figure 2.2** CLSM images of assembled Janus particles showing the cluster identification method.

In addition to assemblies of dimers ( $n = 2$ ), structures with sphere packings ranging from  $n = 3$  to  $n = 7$  can be identified and quantified using image analysis. All scale bars are  $3 \mu\text{m}$ . This figure was originally published in [Shemi, O.; Solomon, M. J. *Langmuir* **2014**, *30*, 15408–15415].

## 2.4 Results

The results yield a comparison of the effect of SAM chemistry and gold layer thickness on Janus particle clusters. Specifically, we first conduct a kinetic study to estimate the time needed for equilibration of the cluster probability distribution after the addition of salt (Sec 2.4.1). That equilibration time is then used as a standard time point to evaluate the degree to which the cluster

probability distribution is affected by NaCl concentration (Sec 2.4.2). Based on the results of the electrolyte study, a particular concentration of electrolyte is chosen to quantify the effects of SAM hydrophobicity and chain length (Sec 2.4.3), and of gold hemisphere thickness (Sec 2.4.4) on the cluster probability distribution. The cluster probability distribution is here defined as the normalized probability of finding a Janus sphere in a cluster of a particular number of spheres.

#### **2.4.1 Effect of time on cluster probability distribution**

The effect of wait time after the addition of salt on cluster growth and equilibrium was studied for PS-Au Janus spheres with a 40 nm Au hemisphere functionalized with hydrophilic MOA. The salt concentration was 3 mM and the initial volume fraction of particles was  $1.0 \times 10^{-5}$ . Figure 2.3 plots the measured cluster distribution at a number of waiting times ranging from 15 min to 240 min. The cluster distribution is here defined as the normalized probability of a Janus particle being located in a cluster of number ranging from  $n = 1$  to  $n = 7$ . In this and following plots, a category for  $n = 8$  or greater (plotted as  $n = 8+$ ) is also included to properly account for the occasional larger cluster observed during the experiments.

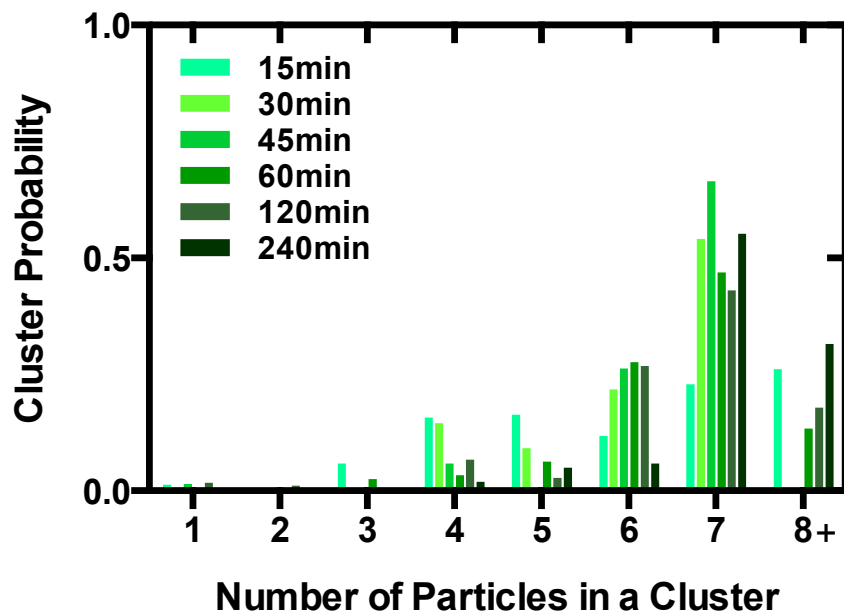


*Figure 2.3 Clustering kinetics of Janus particles.*

The Janus spheres are functionalized with MOA, and the gold hemisphere thickness is 40 nm. The solution contains 3 mM NaCl. This figure was originally published in [Shemi, O.; Solomon, M. J. *Langmuir* **2014**, *30*, 15408–15415].

Figure 2.3 shows that for  $t < 60$  min there are small clusters with a sphere packing of  $n \leq 4$  that initially form and then decrease in quantity as the wait time increases to greater than 60 min. Therefore, at early times there are few large clusters with a sphere packing of  $n > 4$ . However, the abundance of these large number clusters increases at later times. By  $t = 60$  min and greater the cluster distribution evolves only very slowly with time; the kinetics appear to reach steady-state behavior. There is a peak cluster probability that progressively shifts from about  $n = 4$  to 5 at short times to  $n = 7$  at longer times. This transition in the cluster probability distribution happens at about  $t \sim 45$  min. For  $t = 60$  min and greater, out to 240 min, the modal  $n$  is about 7.

Multiple factors should be considered in selecting a characteristic time point and quantification of cluster size distribution for the comparative study of the effect of salt, SAM

chemistry, and gold layer thickness. First, sufficient time is required for Janus particles and clusters to encounter each other and bind. Second, because the Janus particles are not density matched with the solvent ( $\Delta\rho/\rho \sim 2$ ) and because the clusters of different  $n$  are different sizes, clusters sediment at different rates; sufficient time is therefore required for clusters of different size to sediment to the bottom cover slip where observations are made. To account for this effect,  $N_{total}$  used in the construction of the probability distributions is determined directly from the images, so as to provide a local measurement. The results suggest that these two factors are addressed for  $t = 60$  min and greater. Thus,  $t = 60$  min is a suitable time point to study the effects of salt concentration, surface functionality, and gold hemisphere thickness.

#### **2.4.2 Effect of salt concentration on cluster probability distribution**

The effect of four different salt concentrations – 1 mM, 2 mM, 2.5 mM, and 3 mM – on the cluster probability distribution was studied for the case of MOA-modified 40 nm Au hemispheres on PS-Au Janus spheres. The MOA monolayer has a negatively charged functional group. In Figure 2.4, CLSM images of Janus spheres with hydrophilic MOA functionality show a significant effect of salt on clustering. Qualitatively, the distribution of cluster sizes shifts toward higher sphere packings as the salt concentration is increased from 1 mM to 3 mM as shown in Figure 2.4a-d. Specifically, only individual spheres are present in the suspension with 1 mM added salt. For the condition of 2 mM and 2.5 mM NaCl, a range of different sphere packings was observed. Nevertheless, individual (i.e. monomeric) Janus spheres are still the predominant population. For the Janus particle suspension with 3 mM NaCl added, most of the Janus spheres are incorporated in cluster assemblies of  $n = 5$  to  $n = 7$ . At this condition, very few Janus spheres are monomeric.

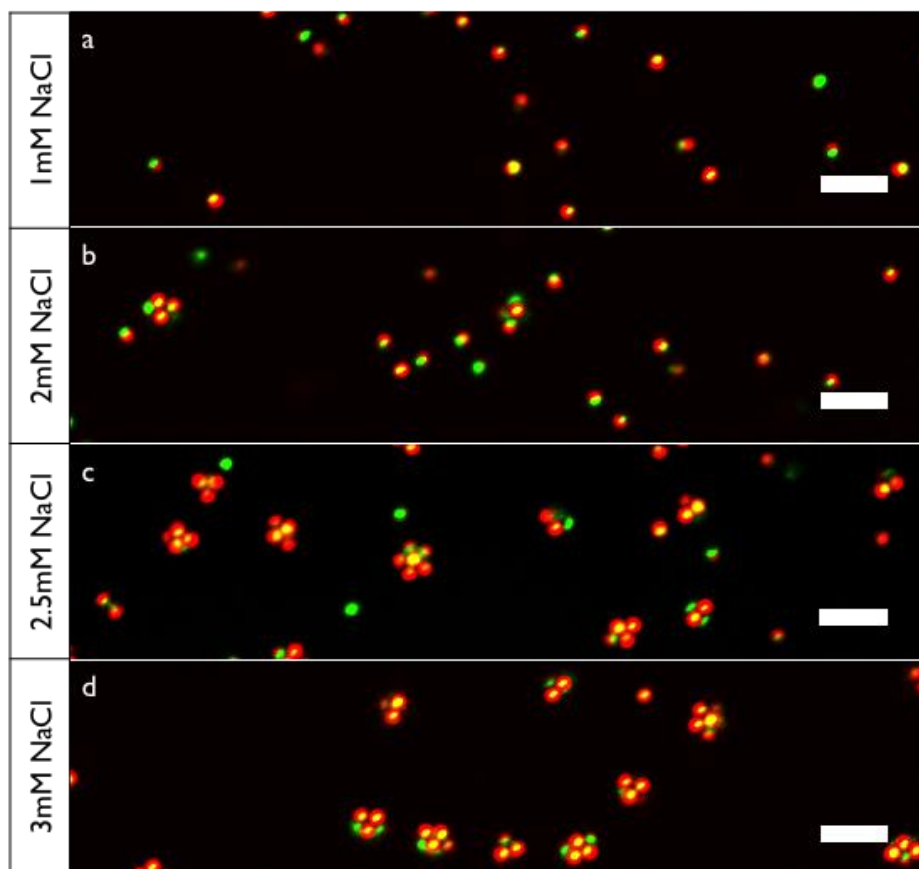


**Figure 2.4** CLSM images of assembled Janus particles at 1, 2, 2.5, and 3 mM NaCl taken at  $t = 60$  min.

The cluster probability shifts to higher sphere packings as the salt concentration is increased. The Janus spheres are functionalized with MOA, and the gold hemisphere thickness is 40 nm. The scale bar is 5 μm. This figure was originally published in [Shemi, O.; Solomon, M. J. *Langmuir* **2014**, *30*, 15408–15415].

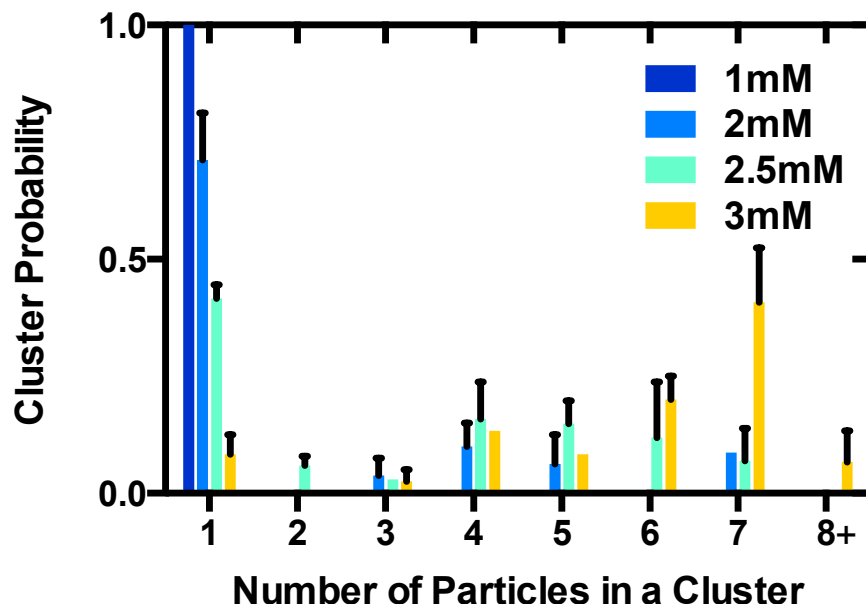


**Figure 2.5** Cluster probability distribution at a fixed hemispheric gold thickness (40 nm) and SAM surface chemistry (MOA) as a function of NaCl at  $t = 60$  min.

An increasing concentration of NaCl results in an increase in the sphere packing of large clusters ( $n > 4$ ), and at 3 mM, the cluster probability of  $n = 7$  spheres is the highest. This figure was originally published in [Shemi, O.; Solomon, M. J. *Langmuir* **2014**, *30*, 15408–15415].

Figure 2.5 shows a plot of the cluster probability distribution for NaCl concentrations varying from 1 – 3 mM with MOA-modified 40 nm gold-coated Janus spheres, as quantified from a series of images such as shown in Figure 2.4. At 1 mM, 100% of the Janus spheres are monomeric. At 2 mM, approximately 70% of the suspension is individual Janus spheres. There is a low abundance of clusters of different  $n$ , with clusters as large as  $n = 7$  observed. The cluster probability distribution at 2.5 mM was comparable to 2 mM – results for 2 mM and 2.5 mM were consistently within about one standard deviation of each other. At the 3 mM NaCl condition,

approximately 40% of Janus spheres were incorporated into clusters of  $n = 7$  spheres, 20% of Janus particles in cluster packings of  $n = 6$ , and  $\sim 15\%$  packings of  $n = 4$ . The abundance of each of the other cluster sizes was significantly less.

From the results in Figure 2.4 and 2.5, we conclude that a salt concentration of 3 mM yields a cluster probability distribution for which the dominant abundance is in the range  $n = 4$  to  $n = 7$ . Because this range of sphere packings is well suited to our cluster observation and characterization method by confocal microscopy, we choose 3 mM salt at which to compare the effect of SAM hydrophobicity and chain length, as well as gold layer thickness, as discussed in the next sections. Other 40 nm Au-coated Janus spheres with varied thiol functionality were studied under analogous conditions of added salt (see Appendix A.3). The transition from predominantly monomeric Janus spheres to clustered spheres also occurred at  $[\text{NaCl}] \sim 3$  mM at these conditions as well. These observations further support the selection of 3 mM for comparative studies of Janus sphere hydrophobicity and gold layer thickness.

### **2.4.3 Effect of SAM hydrophobicity and chain length on cluster probability distribution**

The effect of four different Au hemisphere surface chemistries – no SAM, OT, MOA, and MHDA – on the cluster probability distribution was studied using 40 nm Au-coated Janus spheres. The salt concentration is 3 mM and the measurement time is 60 min after the addition of salt. In Figure 2.6, CLSM images of Janus spheres with varied Au hemisphere surface chemistries at 3 mM show no significant effect on clustering. Specifically, in Figure 2.6a-c, the Janus spheres with no SAM cluster similarly to those with a SAM comprised of either OT or MOA. The situation in Figure 2.6d is slightly more complex. For these MHDA-modified Janus particles, a few instances of non-specific binding occur, in addition to the Au-to-Au binding that is of interest here. Here



non-specific binding is either Au-to-PS or PS-to-PS binding. Even though there is such non-specific binding, many of the cluster bonds are Au-to-Au, and it is these bonds that provide information about the effect of the MHDA SAM on the preferential binding of Janus spheres.

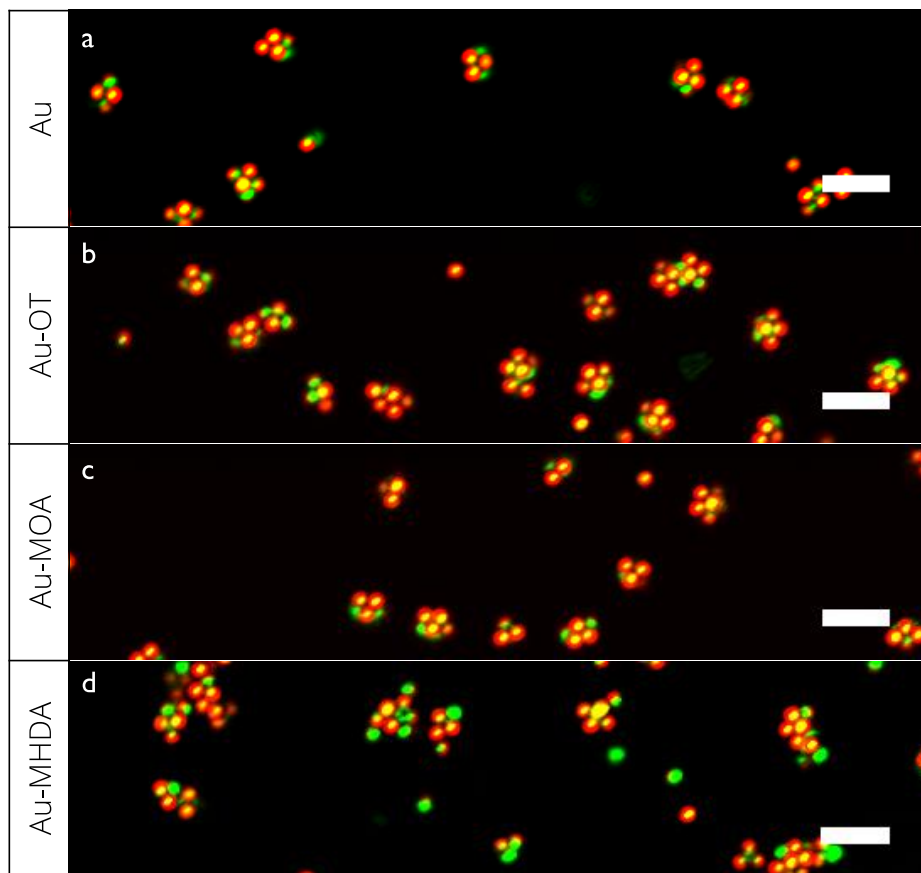


**Figure 2.6** CLSM images of assembled Janus particles at 3 mM NaCl.

(a) Janus spheres with no SAM functionalization, (b) Au-OT-, (c) Au-MOA-, and (d) Au-MHDA-treated gold hemispheres taken at  $t = 60$  min. The cluster probability distributions are similar for all four conditions with one exception for the MHDA condition. With MHDA, both specific Au-to-Au and nonspecific Au-to-PS and PS-to-PS binding is observed, as discussed in the text. The scale bar is 5  $\mu\text{m}$ . This figure was originally published in [Shemi, O.; Solomon, M. J. *Langmuir* **2014**, *30*, 15408–15415].

The measured cluster probability distribution for different thiol functionalities at 3mM added salt is shown in Figure 2.7. The data show that the cluster probability distributions for the four different particle types are very similar. Based on the results in Figure 2.6 and 2.7, we conclude that the variability of SAM hydrophobicity – which spans contact angles that vary by as much as  $90^\circ$  – does not significantly affect the clustering or cluster probability distribution of PS-Au spheres in this electrolyte solution.

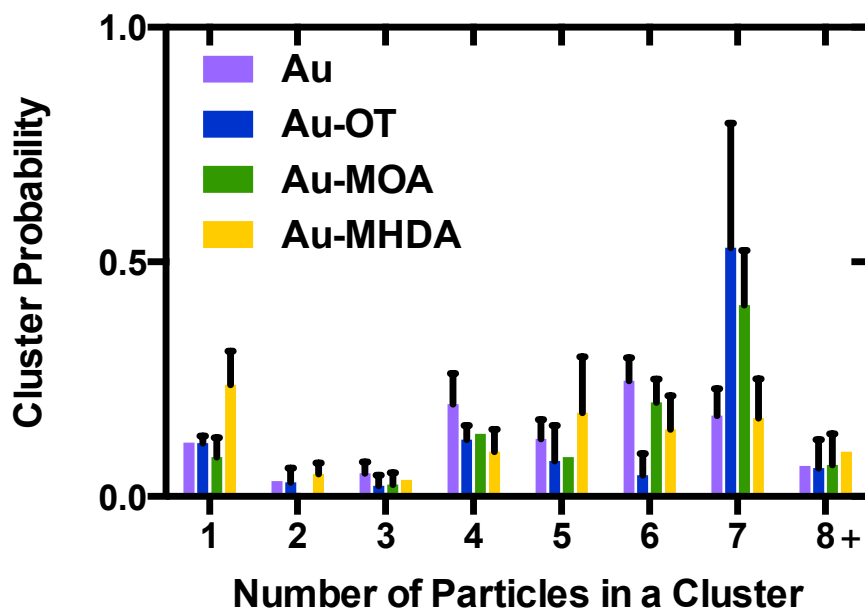


*Figure 2.7 Cluster probability distribution at a fixed hemispheric gold thickness (40 nm) and NaCl concentration (3 mM) as a function of SAM surface chemistry.*

Au without SAM, Au-OT, Au-MOA, and Au- MHDA. This figure was originally published in [Shemi, O.; Solomon, M. J. *Langmuir* 2014, 30, 15408–15415].

The results of Figure 2.6 and 2.7 are for the case of Janus particles with a 40 nm gold layer. To address if the insensitivity of clustering to thiol functionalization extends to other thicknesses of the gold layer, we performed the same set of experiments (at 3 mM NaCl concentration) for the

case of Janus particles with a 10 nm gold layer. A 10 nm layer thickness was chosen because it is a lower bound of the metallic layer thickness that has been studied in the literature<sup>10,14</sup>. The results showed no clustering for any of the SAM layers studied here (Au-OT, Au-MOA, and Au-MHDA) as well as for bare gold particles. That is, all spheres remained in a monomeric state. The significance of this result is discussed in the next section.

#### **2.4.4 Effect of gold layer thickness on cluster probability distribution**

The effect of three different gold layer thicknesses – 10 nm, 20 nm, and 40 nm – on self-assembly and cluster probability distribution was studied using negatively charged MOA-modified Janus particles at 3 mM NaCl. Figure 2.8 shows that the self-assembly propensity of the 10 nm coated spheres is very limited at 3mM NaCl; nearly all particles are present only in monomeric form. At 20 nm, clusters of size  $n = 2$  to 7 are present. At 40 nm,  $n = 7$  cluster sizes are now abundant.

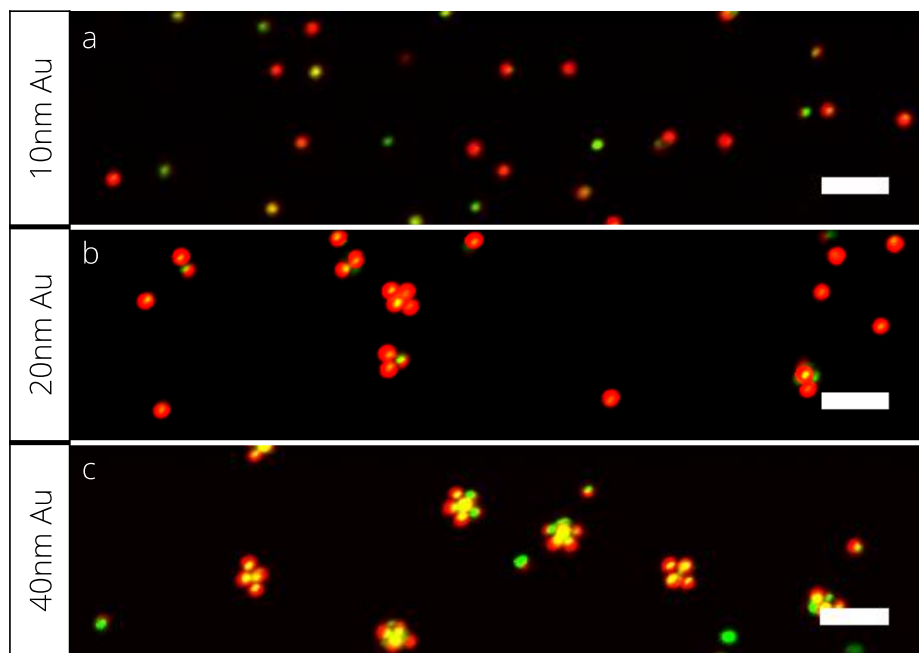


**Figure 2.8** CLSM images of assembled Janus particles with MOA functionality at 3 mM NaCl.

(a) 10, (b) 20, and (c) 40 nm gold hemisphere thicknesses taken at  $t = 60$  min. Janus spheres with a 10 nm gold coating showed essentially no clustering; spheres with a 20 nm gold coating showed a few particles cluster with varied sphere packings, and with 40 nm gold hemispheres, the cluster probability distribution consists mainly clusters of  $n = 7$  spheres. The scale bar is 5  $\mu\text{m}$ . This figure was originally published in [Shemi, O.; Solomon, M. J. *Langmuir* **2014**, *30*, 15408–15415].

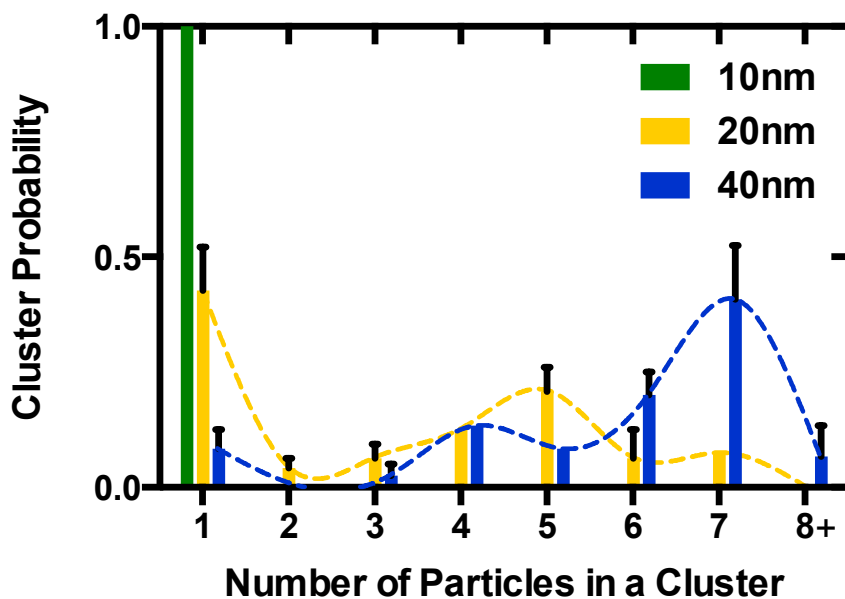


**Figure 2.9** Cluster probability distributions at a fixed SAM functionality (MOA) and NaCl concentration (3 mM) as a function gold layer thickness.

Decreasing the thickness of the gold layer results in a decrease in the binding affinity of PS-Au spheres. This figure was originally published in [Shemi, O.; Solomon, M. J. *Langmuir* **2014**, *30*, 15408–15415].

Figure 2.9 plots the measured cluster probability distribution for the three cases studied – Janus layer thicknesses of 10 nm, 20 nm, and 40 nm. Janus spheres with 10 nm Au layers are monomeric in 3 mM salt. Janus spheres with 20 nm Au hemispheres yielded a distribution of cluster sizes at 3 mM. About 45% of Janus spheres were monomeric, ~20% were packed in clusters of  $n = 5$  spheres, and the remainder were distributed among the packing numbers. The 40 nm thickness of Au yielded a cluster probability distribution of less than 10% each of monomeric spheres and clusters of  $n = 5$  spheres. The mode of this distribution was at  $n = 7$ , with approximately 40% of the 40 nm Janus particles at that condition. These results suggest that the 40 nm has better binding affinity under the same salt condition than either 20 nm or 10 nm. The earlier reported results that Au (10 nm)-PS Janus spheres with varied SAM functionality –

unmodified, OT-modified, MHDA-modified, in addition to MOA-modified – showed no binding under all cases, further supports the higher binding affinity of the 40 nm Janus particles. Although we do not necessarily rule out some effect of SAM functionality for Au layer thickness of 10 nm and 40 nm, the effect of changing the gold layer thickness from 10 nm to 40 nm dominates any effect of such SAM functionalization.

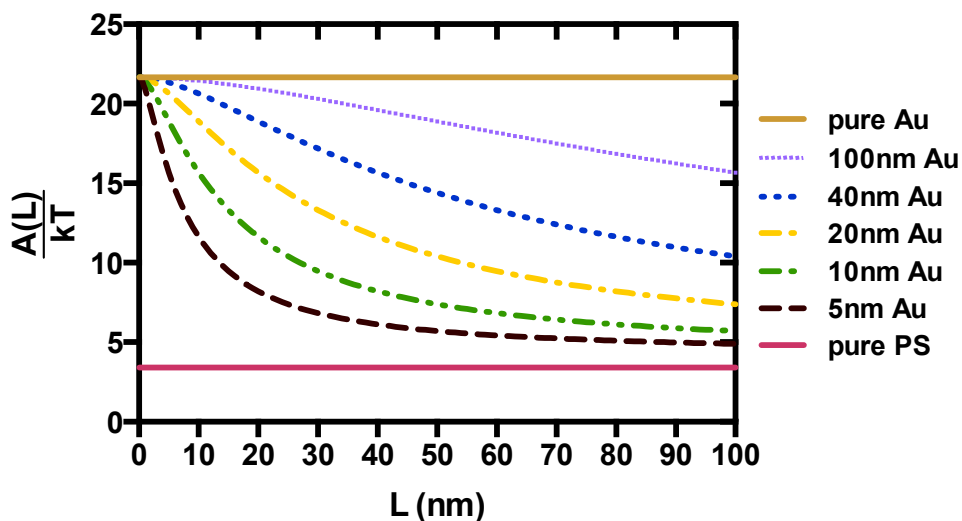


**Figure 2.10** Separation-dependent nonretarded Hamaker coefficients for various thicknesses of the Au layer on polystyrene (PS), compared to the case of pure PS and pure Au.

The calculation is for the interaction across water in a gap of separation  $L$ . This figure was originally published in [Shemi, O.; Solomon, M. J. *Langmuir* **2014**, *30*, 15408–15415].

To understand the origin of the Au thickness effect on clustering, we calculate the separation-dependent Hamaker coefficient for a multilayer system of a gold layer deposited on polystyrene and in contact with water using the theory explained by Parsegian and others<sup>23,24</sup> given literature data for the frequency dependent dielectric functions of polystyrene, gold, and water<sup>25</sup>. Details of this calculation are provided in the SI. The separation-dependent nonretarded Hamaker coefficients,  $A(L)$ , scaled by the thermal energy,  $kT$ , for layered systems of various Au thicknesses,

are shown in Figure 2.10. Results for Au layer thicknesses varying from 5 nm to 100 nm are plotted to show the trend between the pure PS and pure Au limits, which are also plotted.  $A(L)$  provides a characteristic magnitude of the attraction between the gold-layered surfaces. The results show a significant decrease in attraction of the Au layers on PS relative to pure Au, and this effect becomes larger as the Au layer thickness decreases.

In comparing the trends of Figure 2.10 to the trends of the experiments, it is clear that the deviation from the pure Au-to-Au attraction across water becomes significant for all distances greater than 5 nm. For example, at surface separation  $L = 10$  nm, the attraction of a 40 nm gold layer is 30% greater than the 10 nm layer. At a surface separation  $L = 40$  nm, the corresponding attraction is 60% greater. Given the Debye lengths implied by the electrolyte concentrations studied, which is for example  $\sim 6$  nm at 3 mM NaCl, the affinity at separations of these scales appears germane to the observed Au-to-Au binding.

## 2.5 Discussion

The data demonstrate that varying the thickness of the Au layer of PS-Au Janus particles affects their propensity for self-assembly and clustering. Because the tendency of Janus particles to assemble and cluster is a consequence of the pair interactions between them, we infer that the Au layer thickness is a key determinant of the pair interactions between the metallic hemispheres of Janus colloids. Because of the very different effects of Au thickness and SAM hydrophobicity on Janus particle cluster, the work furthermore yields insight about which forces dominate the colloidal interactions of metalodielectric spheres.

In our kinetic study, clusters of different sphere packing sediment at variable rates and exhibited variable degrees of Brownian motion. An equilibrium time of approximately  $t = 60$  min

after the addition of NaCl was sufficient for both the dynamics of pair binding and of cluster sedimentation to occur. It is possible that lower salt concentrations might yield kinetics on time scales slower than those investigated here; however, this possibility does not impact the fact that pair interactions due to hydrophobicity, screened electrostatics, and dispersion forces mediate cluster formation on the time scales and salt concentrations that have been here studied.

Increasing the NaCl concentration increased the population of larger cluster sizes at fixed hemispheric gold thickness (40 nm) and Au-MOA surface chemistry. This change is consistent with the effects of charge screening. Increased salt decreases the range of the electrostatic repulsion, thereby allowing attractive interactions such as hydrophobicity and van der Waal dispersion forces to increasingly dominate at small distances. Previous work has shown that very high concentrations of salt can lead to non-specific binding – either PS-to-PS or Au-to-PS hemispheres – of the Janus particles<sup>26</sup>. Because our focus is Au-to-Au hemispheric interactions, we avoided such high salt concentrations in this study. Only one condition (that of Au-MHDA Janus spheres in 3 mM salt) generated any appreciable non-specific binding in this study.

Changing SAM functionality so as to vary the contact angle wettability from 26° to 115° generated no significant difference in the measured cluster probability distributions. The control – no SAM functionality on the Au hemisphere – also did not differ from the various SAM conditions. At a fixed chain length but differing functional group, the hydrophobic Au-OT Janus spheres produced the same modal cluster probability as hydrophilic Au-MOA Janus spheres at  $n = 7$ . When the Au-MOA hydrophilicity is conserved and the hydrophobic chain length is doubled, the resultant Au-MHDA Janus spheres exhibited similar cluster probability distributions.

Hong et al previously reported that Janus particles with a positively charged monolayer on the Au hemisphere and a negatively charged stabilizer on the PS hemisphere exhibited enhanced



Au-to-PS binding<sup>18</sup>. This enhanced Au-to-PS binding yields clustering and assembly that is controlled by the charge asymmetry of the cluster. In comparison, this study focused on the Au-to-Au bond of Janus particles, finding that varying gold surface hydrophobicity with the aim of increasing the propensity for Au-to-Au binding does not significantly affect the clustering or cluster probability distribution of PS-Au Janus spheres.

While clustering occurs independent of the chemistry of the SAM on the Au hemisphere, lowering Au thickness has a strong effect on clustering. At our highest salt concentration, there were no assemblies observed using a 10 nm hemispheric Au coating. This result was found for all the different thiol functionalizations studied. At the intermediate thickness of 20 nm, the sample remained predominantly monomeric and appreciable amounts of clusters of  $n = 4$  and  $n = 5$  was also observed. In contrast, at 40 nm the modal cluster probability was  $n = 7$  spheres. This progression indicates that the propensity for Au-to-Au binding depends sensitively on the thickness of the metallic layer deposited on the hemisphere.

The magnitude of the competing dispersion forces that generate the van der Waals interaction leads to an Au-to-Au attraction that is apparently stronger than either the PS-to-PS or the Au-to-PS attraction. Moreover, because the van der Waals dispersion force between two bodies depends on the dielectric and conductive properties of the respective volumes, it is plausible that the metal to latex balance within each of the volumes will modulate the strength of the interaction. Evidence for an effect of layer thickness on van der Waals interaction is available in the literature<sup>17,23,27</sup>. These sources provide an explanation of attraction of layered bodies that is applicable to the observations of this paper, because for the systems studied, thin film effects transition toward bulk effects on scales  $\sim 5 - 100$  nm. Indeed, separation dependent Hamaker constant calculations for the polystyrene-gold-water system (Figure 2.10) confirm that there is a

significant deterioration of the attraction for separations beginning in the range of 5 – 25 nm for Au layer thicknesses in the range of 10-40 nm, and that this decrease in attraction becomes more pronounced as the gold layer thickness is decreased.

Thus, we conclude that in the experiments the Au layer thickness modulates the strength of van der Waals forces, thereby affecting the propensity of Janus particles to assemble into clusters. Specifically, at 40 nm, the gold layer dominates, generating a strong van der Waals interaction. At 10 nm, the contribution of the gold is less. There is a greater contribution from the polystyrene underneath, and the van der Waals interaction is subsequently weaker. Consequently, van der Waals interactions of the metallic layer affect cluster assembly to a much greater degree than hydrophobic interactions. Therefore, parameterization and control of the metallic van der Waals interactions of Janus particles should prove helpful to both experimental and simulation studies of their self-assembly.

## **2.6 Conclusion**

We have reported the contributions of kinetics, salt concentration, SAM hydrophobicity and chain length, and metallic layer thickness (between 10 and 40 nm) on the cluster probability distributions of Janus spheres comprised of polystyrene and gold. Two-channel CLSM confirmed the dominance of Au-to-Au binding and allowed the identification of the abundance of clusters of different number of spheres. This analysis demonstrated the effect of the surface chemistry of the Janus colloids on self-assembly and clustering. The introduction of thiol functionalization of the Au hemisphere changed the wettability/hydrophobicity of the Au surface, as demonstrated by contact angle measurements. However, the results of self-assembly are independent of the different SAM chemistries tested for gold layer thicknesses of 40 nm and 10 nm. They are however,

strongly linked with the thickness of the Au layer on the Janus particle. Calculations of the separation dependent Hamaker constant support an effect of Au-layer thickness on attractions in the system for the gold-layer thicknesses investigated. Our observations therefore show that metallic layer thickness is more influential than hydrophobic interactions in determining the binding affinity of metallodielectric Janus particles. The implication is van der Waals dispersion forces dominate hydrophobic forces in mediating the pair binding of these particles.

## 2.7 References

1. Glotzer, S. C.; Solomon, M. J. Anisotropy of Building Blocks and Their Assembly into Complex Structures. *Nat. Mater.* **2007**, *6* (8), 557–562.
2. Nisisako, T.; Torii, T.; Takahashi, T.; Takizawa, Y. Synthesis of Monodisperse Bicolored Janus Particles with Electrical Anisotropy Using a Microfluidic Co-Flow System. *Adv. Mater.* **2006**, *18* (9), 1152–1156.
3. Lahann, J. Recent Progress in Nano-Biotechnology: Compartmentalized Micro- and Nanoparticles via Electrohydrodynamic Co-Jetting. *Small* **2011**, *7*, 1149–1156.
4. Jiang, S.; Chen, Q.; Tripathy, M.; Luijten, E.; Schweizer, K. S.; Granick, S. Janus Particle Synthesis and Assembly. *Adv. Mater.* **2010**, *22* (10), 1060–1071.
5. Pawar, A. B.; Kretschmar, I. Patchy Particles by Glancing Angle Deposition. *Langmuir* **2008**, *24*, 355–358.
6. Smoukov, S. K.; Gangwal, S.; Marquez, M.; Velev, O. D. Reconfigurable Responsive Structures Assembled from Magnetic Janus Particles. *Soft Matter* **2009**, *5* (6), 1285.
7. Howse, J.; Jones, R.; Ryan, A.; Gough, T.; Vafabakhsh, R.; Golestanian, R. Self-Motile Colloidal Particles: From Directed Propulsion to Random Walk. *Phys. Rev. Lett.* **2007**, *99* (4), 48102.
8. Hong, L.; Cacciuto, A.; Luijten, E.; Granick, S. Clusters of Amphiphilic Colloidal Spheres. *Langmuir* **2008**, *24* (3), 621–625.
9. Gangwal, S.; Cayre, O. J.; Velev, O. D. Dielectrophoretic Assembly of Metallodielectric Janus Particles in AC Electric Fields. *Langmuir* **2008**, *24*, 13312–13320.
10. Chen, Q.; Bae, S. C.; Granick, S. Directed Self-Assembly of a Colloidal Kagome Lattice. *Nature* **2011**, *469* (7330), 381–384.

11. Solomon, M. J. Directions for Targeted Self-Assembly of Anisotropic Colloids from Statistical Thermodynamics. *Curr. Opin. Colloid Interface Sci.* **2011**, *16*, 158–167.
12. Whitesides, G.; Grzybowski, B. Self-Assembly at All Scales. *Science* **2002**, *295*, 2418–2421.
13. Wu, L. Y.; Ross, B. M.; Hong, S.; Lee, L. P. Bioinspired Nanocorals with Decoupled Cellular Targeting and Sensing Functionality. *Small* **2010**, *6* (4), 503–507.
14. Chen, Q.; Whitmer, J. K.; Jiang, S.; Bae, S. C.; Luijten, E.; Granick, S. Supracolloidal Reaction Kinetics of Janus Spheres. *Science* **2011**, *331* (6014), 199–202.
15. Russel, W. B.; Saville, D. A.; Schowalter, W. R. *Colloidal Dispersions*; **1989**; pp. 88–160.
16. Israelachvili, J. N. *Intermolecular and Surface Forces*; **2011**; pp. 253–340.
17. Walsh, R. B.; Nelson, A.; Skinner, W. M.; Parsons, D.; Craig, V. S. J. Direct Measurement of van Der Waals and Diffuse Double-Layer Forces between Titanium Dioxide Surfaces Produced by Atomic Layer Deposition. *J. Phys. Chem.* **2012**, *116*, 7838–7847.
18. Hong, L.; Cacciuto, A.; Luijten, E.; Granick, S. Clusters of Charged Janus Spheres. *Nano Lett.* **2006**, *6* (11), 2510–2514.
19. Park, B. J.; Brugarolas, T.; Lee, D. Janus Particles at an Oil–water Interface. *Soft Matter* **2011**, *7*, 6413.
20. Bain, C.; Troughton, E.; Tao, Y.; Evall, J.; Whitesides, G.; Nuzzo, R. Formation of Monolayer Films by the Spontaneous Assembly of Organic Thiols from Solution onto Gold. *J. Am. Chem. Soc.* **1989**, *335*, 321–335.
21. Ulman, A. Formation and Structure of Self-Assembled Monolayers. *Chem. Rev.* **1996**, *96*, 1533–1554.
22. Manoharan, V. N.; Elsesser, M. T.; Pine, D. J. Dense Packing and Symmetry in Small Clusters of Microspheres. *Science* **2003**, *301*, 483–487.
23. Parsegian, V. A. Reconciliation of van Der Waals Force Measurements between Phosphatidylcholine Bilayers in Water and between Bilayer-Coated Mica Surfaces. *Langmuir* **1993**, *9*, 3625–3628.
24. Gingell, D.; Parsegian, V. A. Prediction of van Der Waals Interactions Between Plastics in Water Using the Lifshitz Theory. **1973**, *44*, 456–463.
25. Parsegian, V. A.; Weiss, G. H. Spectroscopic Parameters for Computation of van Der Waals Forces. *J. Colloid Interface Sci.* **1981**, *81*, 285–289.

26. Shah, A. a; Schultz, B.; Kohlstedt, K. L.; Glotzer, S. C.; Solomon, M. J. Synthesis, Assembly, and Image Analysis of Spheroidal Patchy Particles. *Langmuir* **2013**, *29*, 4688–4696.
27. Ederth, T. Computation of Lifshitz - van Der Waals Forces between Alkylthiol Monolayers on Gold Films. *Langmuir* **2001**, *17* (11), 3329–3340.

## CHAPTER 3

### Self-Propulsion of Platinum/Polystyrene Janus Ellipsoids\*\*

#### 3.1 Abstract

The propulsion of platinum coated polystyrene prolate ellipsoids, as generated by reactively induced diffusiophoretic motion, is determined by direct visualization of the trajectories of the active particles. Janus ellipsoids, fabricated from 1.0  $\mu\text{m}$  diameter polystyrene spheres, with aspect ratios ranging from 2.4 to 6.7 and half-coated with platinum along the ellipsoid's major axis, exhibit complex trajectories in aqueous solutions of hydrogen peroxide. As the concentration of hydrogen peroxide is increased in the range of 2-8% (w/v), we observe a transition from three-dimensional passive, Brownian motion to two-dimensional active motion. This transition from passive to active motion is complete by 4% (w/v) hydrogen peroxide. We quantify the effect of particle aspect ratio on the mean-squared displacement and mean-squared angular displacement at 8% (w/v) hydrogen peroxide. The two-dimensional trajectories of the particles were grouped into three categories for more detailed kinetic analysis. In the first category, ballistic ellipsoids translate at least five times more than purely diffusive ellipsoids at the characteristic time scale of rotational diffusion. In the second category, spinning ellipsoids move only short distances with the dominant

---

\*\* This chapter is in preparation for publication by O. Shemi & M.J. Solomon.

motion being rotation about the minor axis over long time scales. A third category captures trajectories that include both significant translation and rotation. We consider the physical origins of the observed categories of motion and extract the forces and torques generated by the catalytically generated propulsion as a function of aspect ratio.

## 3.2 Introduction

Janus colloids are a type of anisotropic particle that incorporate dual interactions, material properties, and/or function<sup>1</sup>. In addition to their use for drug delivery<sup>2</sup> and self-assembly<sup>3,4</sup>, Janus particles can display active motion in low Reynolds number fluid systems. To generate active motion, a hemisphere of the colloidal particle is capped with a layer of platinum<sup>5-8</sup>. This platinum surface of the Janus colloid reacts with a fuel such as hydrogen peroxide,<sup>5,7,9</sup> generating active motion with characteristics similar to the behavior of flagellar bacteria. The phoretic motion is due to the presence of concentration gradients at the particle-solvent interface. These gradients are a consequence of the catalytically induced chemical reaction.<sup>10</sup> This process is a remarkable transformation of the localized availability of chemical energy at the molecular scale into directed motion of particles at the colloidal scale.

Active motion has been observed in colloids of various shapes and Janus anisotropy including polystyrene-platinum spheres<sup>5,11,12</sup>, silica-platinum spheres<sup>9</sup>, and gold-platinum nanorods<sup>7</sup>. These studies have extended the understanding of the translation and rotation that results from the diffusiophoretic motion of Janus particles. Research has shown the effect of a variety of physical properties on this active motion: in the case of spheres<sup>11</sup>, the particle radius determines the drag that balances the active force; the platinum layer thickness<sup>12</sup> determines the particle density, catalytic activity, resistance to flow, all of which affect active motion. Platinum surface

coverage<sup>13</sup> determines the availability of active catalytic sites. This availability influences the localized concentration gradients across the particle that drive the self-diffusiophoresis. Additional understanding of the effect of drag and propulsive forces on active motion may be obtained by systematically varying the shape of the Janus colloids. In this study, we aim to observe the effect of shape on the motility of active Janus particles.

Here we investigate the self-propulsion of prolate Janus ellipsoids with a platinum coating along the major axis. This geometry allows for qualitative and quantitative analysis of rotational and translational motion generated by the localized decomposition of hydrogen peroxide. In addition, through the study's systematic variation of particle aspect ratio (and thereby surface area and topography), these ellipsoids differ from the previously studied cases of spheres and rods in the relative magnitudes of drag and propulsive forces generated by the catalytic activity. The anisotropic landscape of the ellipsoids generates propulsive motion perpendicular to the major axis of the ellipsoid. We find that the dynamic motion of these Janus ellipsoids leads to interesting active trajectories, with varying contributions of translation and rotation<sup>14-16</sup>.

We characterize hydrogen peroxide-induced active motion in Janus ellipsoids as particle aspect ratio is varied between 2.4 and 6.7. The active motion is resolved and quantified by two-channel confocal microscopy and image analysis, respectively. Qualitatively, we find that the transition from three-dimensional diffusion to two-dimensional active motion is reached as hydrogen peroxide concentration is increased to 4%. Both mean squared displacement (MSD) and mean squared angular displacement (MSAD) are quantified at 8% hydrogen peroxide concentration, a condition at which active motion is strongly apparent. Interesting classes of trajectories are reported, including ones that are predominantly translational as well as ones that



are predominantly rotational. The propulsive forces and torques acting on the Janus ellipsoids are extracted from analysis of these types of trajectories.

### **3.3 Materials and Methods**

#### **3.3.1 Janus Ellipsoid Synthesis**

Polystyrene ellipsoids were synthesized as in the literature<sup>17,18</sup>. Briefly, 300 mL of a 2.0 vol% solution of carboxylate-modified polystyrene spheres (PS) (0.99 $\mu$ m, F8821, Life Technologies) is added to 8 ml of 10% Polyvinyl alcohol (PVA) in water solution. The solution is well-mixed before pouring on an OmniTray (Thermo Scientific Nunc OmniTray, 242811) and allowed to dry for 16-24 hrs at room temperature. Once dried, the film is cut into 4 cm x 1 cm strips, assembled and clamped to a device that imposes a uniaxial deformation in a constant temperature oven. To produce the ellipsoids, the films are heated to 120°C, which is above the glass transition temperature of the polystyrene, kept at 120°C for 10 mins, and then uniaxially deformed. The ellipsoid aspect ratio is controlled by the strain of the uniaxial deformation. In this study we produce ellipsoids of aspect ratio  $2.4 \pm 0.4$  (major axis length =  $1.9 \pm 0.2$ , minor axis length =  $0.8 \pm 0.1$ ),  $4.8 \pm 1.0$  (major axis length =  $2.8 \pm 0.4$ , minor axis length =  $0.6 \pm 0.1$ ), and  $6.7 \pm 0.8$  (major axis length =  $3.6 \pm 0.3$ , minor axis length =  $0.5 \pm 0.04$ ) by applying elongation strains of 0.38, 0.56, and 0.65, respectively. Once stretched, the oven is turned off, the films are allowed to cool, and then cut from the clamping apparatus. An approximately ~ 1 cm long section at each end of the film is discarded to account for any inhomogeneous deformation in these regions due to clamping. The stretched films are suspended in DI water and sonicated in a bath sonicator

(Branson Ultrasonics) for one hour. The DI water is then exchanged 5 times using centrifugation to remove the PVA from the particle suspension (5000G for 10min).

The suspension of ellipsoids is then solvent-exchanged with 200 proof ethanol (E7023, Sigma-Aldrich) using centrifugation. These ellipsoids are spin-coated (WS-400B-6NPP, Laurell) onto a glass microscope slide (glass coverslip, 35 mm × 50 mm × 0.13 mm, Fisher Scientific) at 300 rpm for 20 s, then 3000 rpm for 20 s. Next, a 20 nm layer of platinum is deposited along the ellipsoid's long axis via physical vapor deposition (PVD) using an e-beam evaporator (Denton Vacuum). Scanning electron microscopy (SEM) images (Philips XL-30 FEG) of the Janus ellipsoids of different aspect ratios are shown in Figure 3.1(a-c).

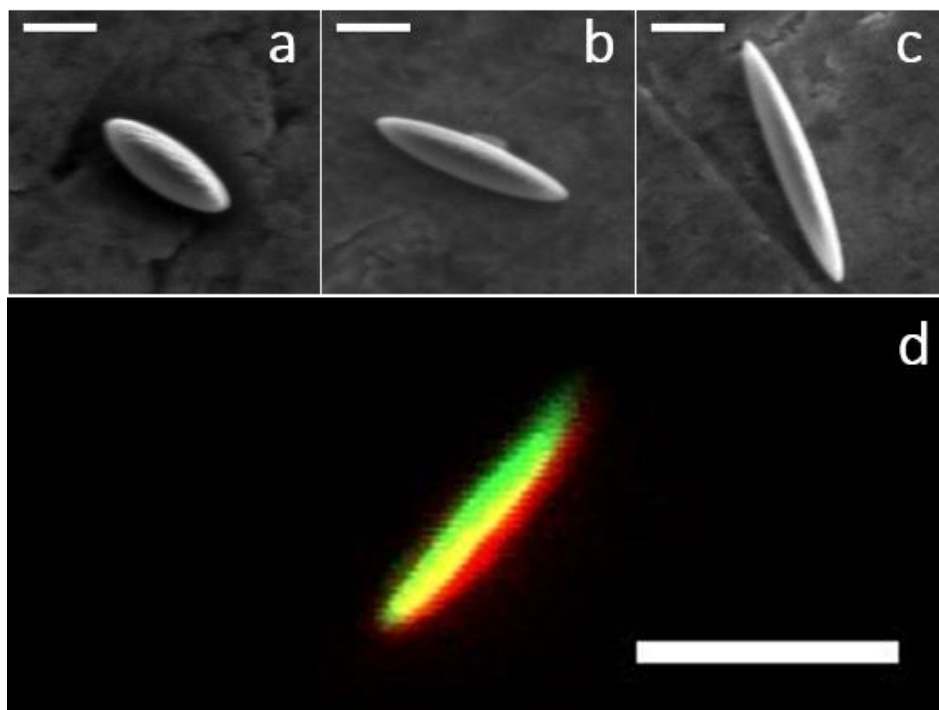


**Figure 3.1** Microscopy images of polystyrene colloidal ellipsoids coated with a 20 nm platinum layer along one-half of the major axis.

The aspect ratio (AR) of the fabricated Janus ellipsoids shown in the SEM images are (a)  $2.4 \pm 0.4$ , (b)  $4.8 \pm 1.0$ , and (c)  $6.7 \pm 0.8$ . The brighter half of the particle is the side with the platinum coating. (d) Two-channel overlay CLSM image of Janus ellipsoid with platinum (green) and polystyrene (red). Scale bars are 1  $\mu\text{m}$  (a-c) and 3  $\mu\text{m}$  (d).

### **3.3.2 Janus Particle Self-Propulsion**

Experiments are conducted in Lab-Tek™ II 8-well chambered cover glass (155409, Fisher Scientific). The wells are pre-cleaned in a photosensitized oxidative chamber (Jelight UVO Cleaner) for 20 min. 150  $\mu$ l of the polystyrene/platinum particles in DI water are transferred to the well; the particles are allowed to sediment for one hour. An equal volume of hydrogen peroxide solution is then added and allowed to mix. The final concentration of the hydrogen peroxide solution is between 2-8% (w/v).

### **3.3.3 Confocal Laser Scanning Microscopy**

Janus particle dynamics are observed by confocal laser scanning microscopy (CLSM, Nikon A1R). Time series of CLSM images were acquired with a 100 $\times$ , 1.4 NA, oil immersion objective. The platinum cap of the Janus ellipsoid is imaged in reflection mode with a 488 nm laser, and the fluorescent polystyrene is imaged with a 561 nm excitation and emission band centered at 570 to 620 nm. The combined two-color image is shown in Figure 3.1d for a representative experiment. The platinum side of the Janus ellipsoid is colored green; the fluorescence of the polystyrene is colored red. 256 x 256 square pixel images were recorded for 30 seconds at a rate for 30 frames per second. A set of reference images of spheres and ellipsoids immobilized on the surface was used to determine the static error<sup>19</sup> of the imaging system.

### **3.3.4 Image Analysis and Particle Tracking**

The centroids and orientation of particles recorded in each frame are determined in ImageJ and analyzed in Matlab. The 2D time series of CLSM images are processed in ImageJ to identify particle centroids and angular orientation (for the ellipsoids) with respect to the lab view plane in each frame, as shown in Figure 3.2. Figure 3.2(a,c) are CLSM images and (b,d) overlay images

after image processing with detection parameters based on pixel size and particle eccentricity. As shown in Figure 3.2b, we are able to detect spheres (blue) while excluding the occasional dimer and other non-spherical shapes (black). We also detect the 2D motion and orientation of ellipsoids (Figure 3.2d).

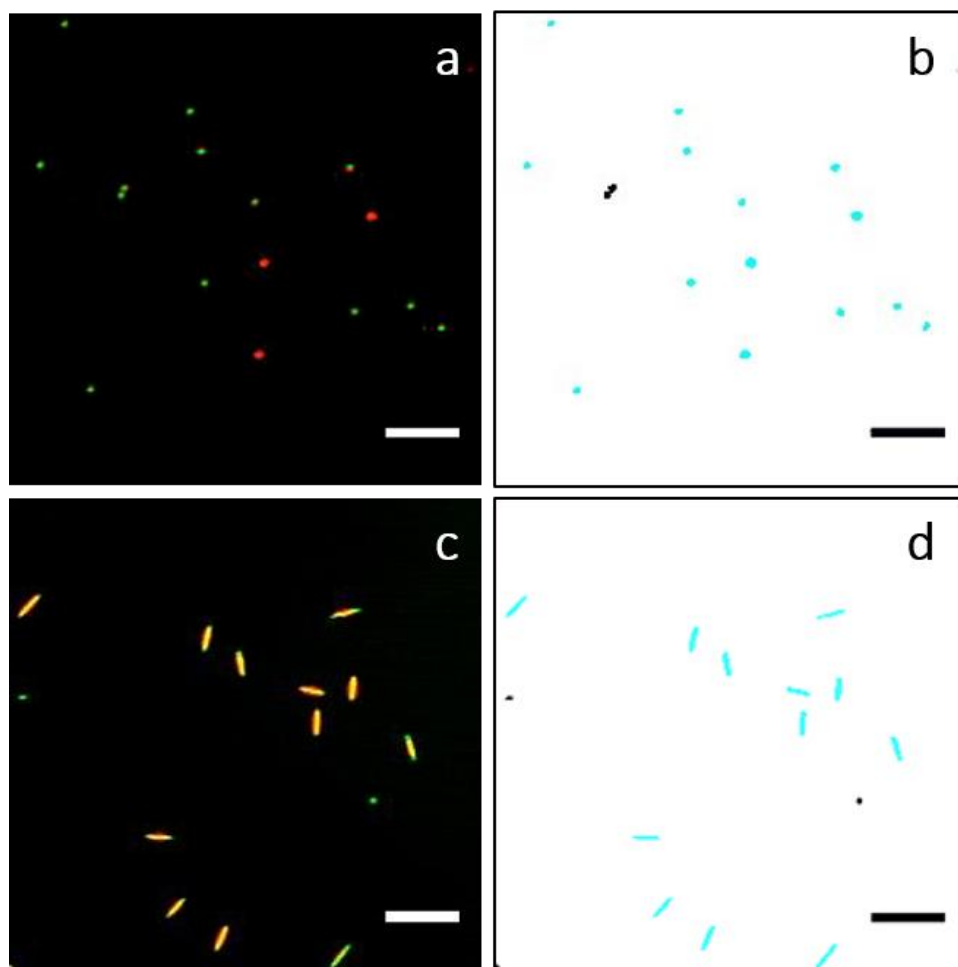


**Figure 3.2 Images of Janus spheres and ellipsoids in suspension.**

CLSM images identify the (a) Janus spheres and (c) Janus ellipsoids. Image processing software can identify particles based on pixel size and eccentricity for (b) spheres and (d) ellipsoids. All scale bars are 10  $\mu\text{m}$ .

The particles are linked from frame to frame to identify individual trajectories using an open source image-processing code Simple Tracker<sup>20</sup>. The code links particles with centroidal distance of 3  $\mu\text{m}$  or less from frame-to-frame. Particles can move out of frame for up to five

consecutive frames and still be assigned as a continuous particle trajectory. We apply the same linking routine to the reference image series of immobile spheres and ellipsoids to characterize the static error in our imaging system.

### 3.4 Results

To establish the performance of the fabricated particles and the imaging system, we first characterize the dynamics of spheres (both passive and active). Figure 3.3 compares the mean-squared displacement (MSD) of homogeneous spheres without hydrogen peroxide, Janus spheres in solutions without hydrogen peroxide, and Janus spheres with hydrogen peroxide, at 8% (w/v). All displacements measured are well above the static error of the imaging system. The plots record the MSD,  $\langle \Delta \vec{r}^2(\Delta t) \rangle = \langle [\vec{r}(t + \Delta t) - \vec{r}(t)]^2 \rangle$ , of all identified particles. The homogeneous spheres are diffusive with a diffusion coefficient  $D = 0.40 \pm 8.0e - 6 \mu m^2/s$ . The Janus spheres in aqueous solution show a MSD with  $D = 0.42 \pm 5.8e - 4 \mu m^2/s$ . The expected value for these particles, from the Stokes-Einstein equation, is  $D = 0.46 \mu m^2/s$ . The Brownian experiments are shown to be in agreement with the expected value at a relative deviation of  $\eta = 0.14$  for isotropic spheres and  $\eta = 0.095$  for Janus spheres.

As described for example in Howse et al<sup>5</sup>, active Janus spheres exhibit complex MSD behavior that transitions from primarily ballistic behavior at short times to effective diffusion at long times. The characteristic time scale for the transition from ballistic motion to effective diffusion, is the inverse of the rotational diffusion coefficient  $\tau_R^{-1} = k_B T / \xi_R$ , where the friction coefficient  $\xi_R$  varies with particle shape, dimension and orientation<sup>21</sup>. By applying the expressions of Howse et al<sup>5</sup>, Janus spheres in 8% H<sub>2</sub>O<sub>2</sub> yield an effective diffusivity,  $D_{\text{eff}} = 0.6 \mu m^2/s$ , an average velocity,  $v = 1.9 \mu m/s$ , and characteristic time scale  $\tau_R = 1.8 s$ . These values are

consistent with literature values. For example, for a 1.0 micron Janus sphere with a 5 nm thick platinum layer in 10% hydrogen peroxide, Howse et al. report  $D = 0.31 \mu\text{m}^2/\text{s}$ ,  $v = 3.1 \mu\text{m}/\text{s}$ , and  $\tau_R = 3.9 \text{ s}$ . Given that our system has lower hydrogen peroxide concentration with a thicker platinum coating, a higher effective diffusivity and decreased velocity and characteristic time scale are consistent with the investigations of others<sup>11,12</sup>.

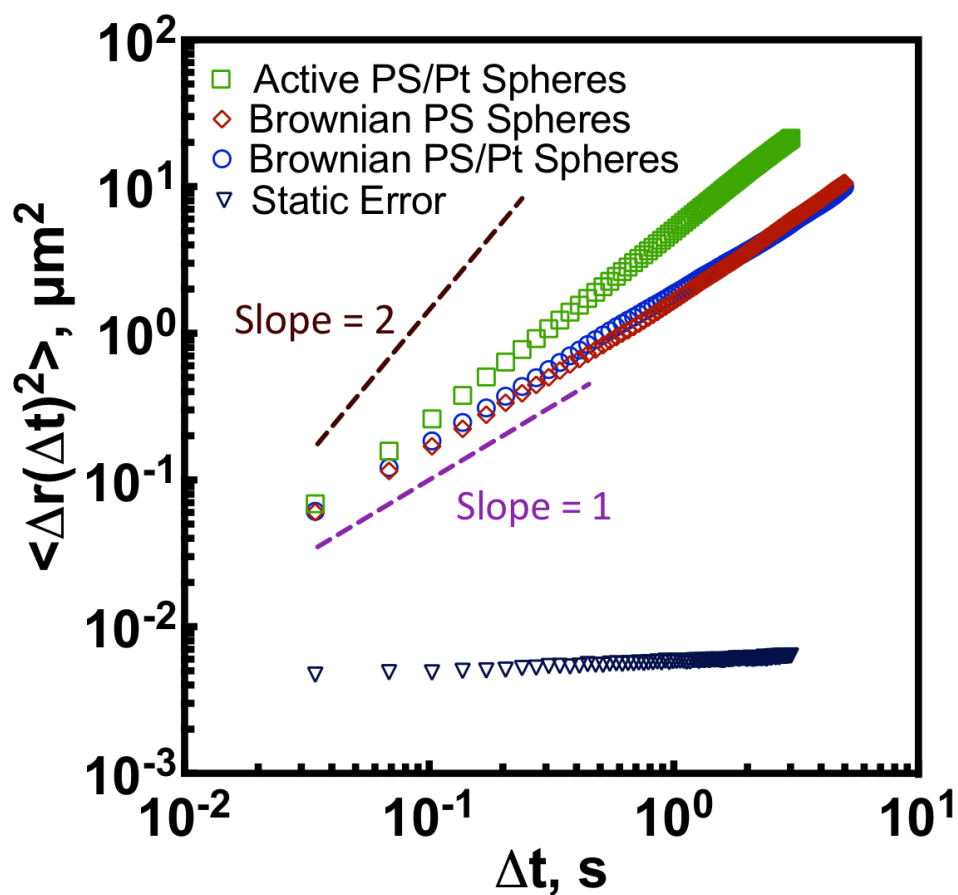


**Figure 3.3 Mobility of spheres in water and 8% (w/v) aqueous hydrogen peroxide solution.**

The MSD  $\langle \Delta r^2(\Delta t) \rangle$  of Brownian PS spheres, Brownian PS-Pt spheres and active PS-Pt spheres in peroxide are given.

The active motion of Janus ellipsoids in an aqueous suspension of 8% (w/v) hydrogen peroxide solution is reported in Figure 3.4. It is representative of the Janus ellipsoids displaying trajectories that vary considerably both from particle to particle and for any given particle over time. A number of particles show ballistic trajectories, with motion perpendicular to the major axis of the particle. Close inspection of these trajectories suggests that the platinum face of the Janus ellipsoid is oriented in the aft position with the polystyrene surface in the fore position. Another set of trajectories show very little translation, but significant rotation. Such particles, which we refer to as spinners, primarily sit at particular locations and rotate. Other particles show trajectories intermediate between these two regimes with transition from one limit to the other over time.

Figure 3.4 shows a time series of CLSM images, a temporal projection, and a centroidal trajectory (a, b, c) of a representative ballistic ellipsoid and (d, e, f) a representative spinning ellipsoid in 8% hydrogen peroxide solution. Figure 3.4a is a time-lapse montage of a ballistic ellipsoid moving left to right in a span of approximately 2 sec. Figure 3.4b shows the overlapping image frames depicting translational and (some) rotational motion of the ballistic spheroid. Figure 3.4c shows the overall centroidal trajectory; over this period the trajectory is ballistic, with minimal reorientation observed. Figure 3.4d is a time-lapse montage of a spinning ellipsoid rotating clockwise for a span of approximately 1 sec. Figure 3.4e is a temporal projection of the frames in Figure 3.4d; the projection indicates that the spinning ellipsoid completes  $\sim 1.6$  rotations in approximately 1 sec. Figure 3.4f shows the overall centroidal trajectory with minimal translation observed. The projections of the ballistic and spinning ellipsoid confirm that the particles propel in a direction perpendicular to the major axis of the particle.

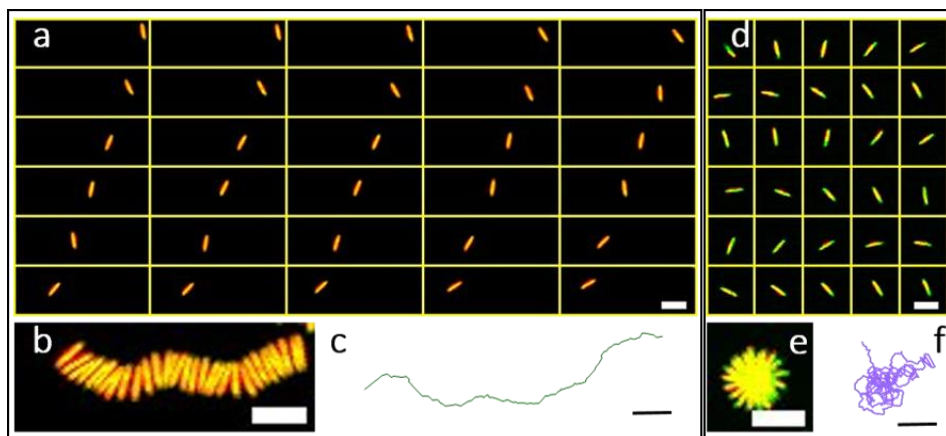


**Figure 3.4** CLSM images and centroidal trajectories of Janus ellipsoids in motion in 8% peroxide.

(a) Time series images of a Janus ellipsoid exhibiting a primarily translational motion (ballistic) in ~2 min with (b) a superimposed time lapse image of the particle and (c) the complete trajectory for the ballistic particle. (d) Time series images of a Janus ellipsoid exhibiting a primarily rotational motion (spinning) in ~1 min with (e) a superimposed time lapse image of the particle and (f) the complete trajectory for the spinning particle. All scale bars are 5  $\mu\text{m}$ .

The orientation of the Janus ellipsoid can be symmetric in the lubrication flow regime which results in ballistic motion, while asymmetry results in repeated spinning of ellipsoids. The matter of symmetry is a result of the gradient profile across the anisotropic particle as shown in Figure 3.5.



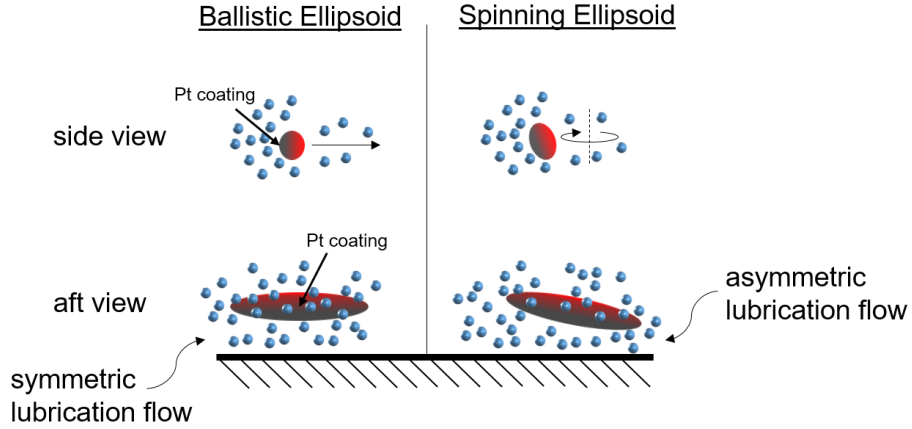


**Figure 3.5** Illustration of active Janus ellipsoid moving near the coverslip.

To characterize the effect of particle shape on active motion, we compare average measures of centroidal displacement and angular rotation. As shown in Figure 3.6,  $\vec{r}(\Delta t)$  gives the displacement of the ellipsoid over a time interval,  $\Delta t = t_1 - t_0$ , from the laboratory frame centroid positions of the ellipsoids given by  $(x_0, y_0)$  and  $(x_1, y_1)$ . The orientation of the ellipsoid,  $\theta$ , is defined as the angle between the vector  $\hat{u}$  normal to the particle's major axis and a vector defining the laboratory reference frame. The angular displacement is given by the MSAD relation,  $\langle \Delta \vec{\theta}^2(\Delta t) \rangle = \langle [\vec{\theta}(t + \Delta t) - \vec{\theta}(t)]^2 \rangle$ . The MSD  $\langle \Delta \vec{r}^2(\Delta t) \rangle$  and MSAD  $\langle \Delta \vec{\theta}^2(\Delta t) \rangle$  are calculated for two-dimensional translation motion and rotational motion, respectively.

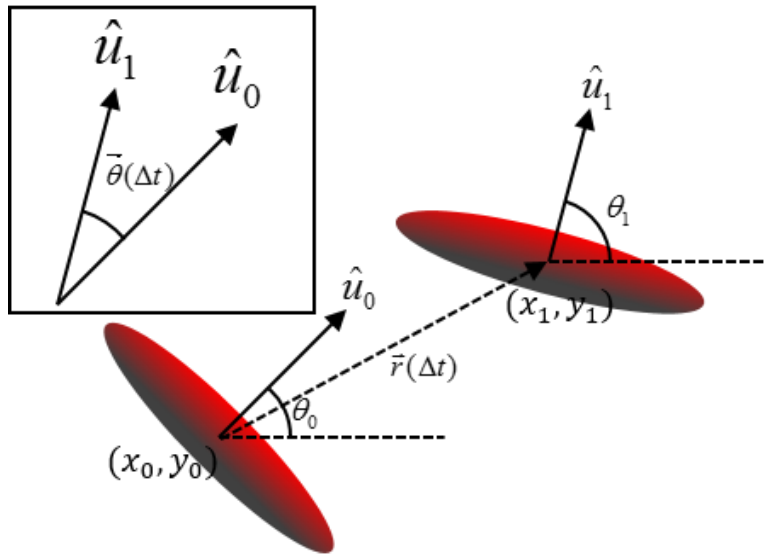


***Figure 3.6 Schematic of the ellipsoidal particle motion over a time interval and the parameters used to characterize its displacement.***

The two-dimensional translational motion is determined by the displacements of its centroid. The two-dimensional angular displacement is determined by change in orientation angle with respect to laboratory reference frame. Variables are as defined in the text.

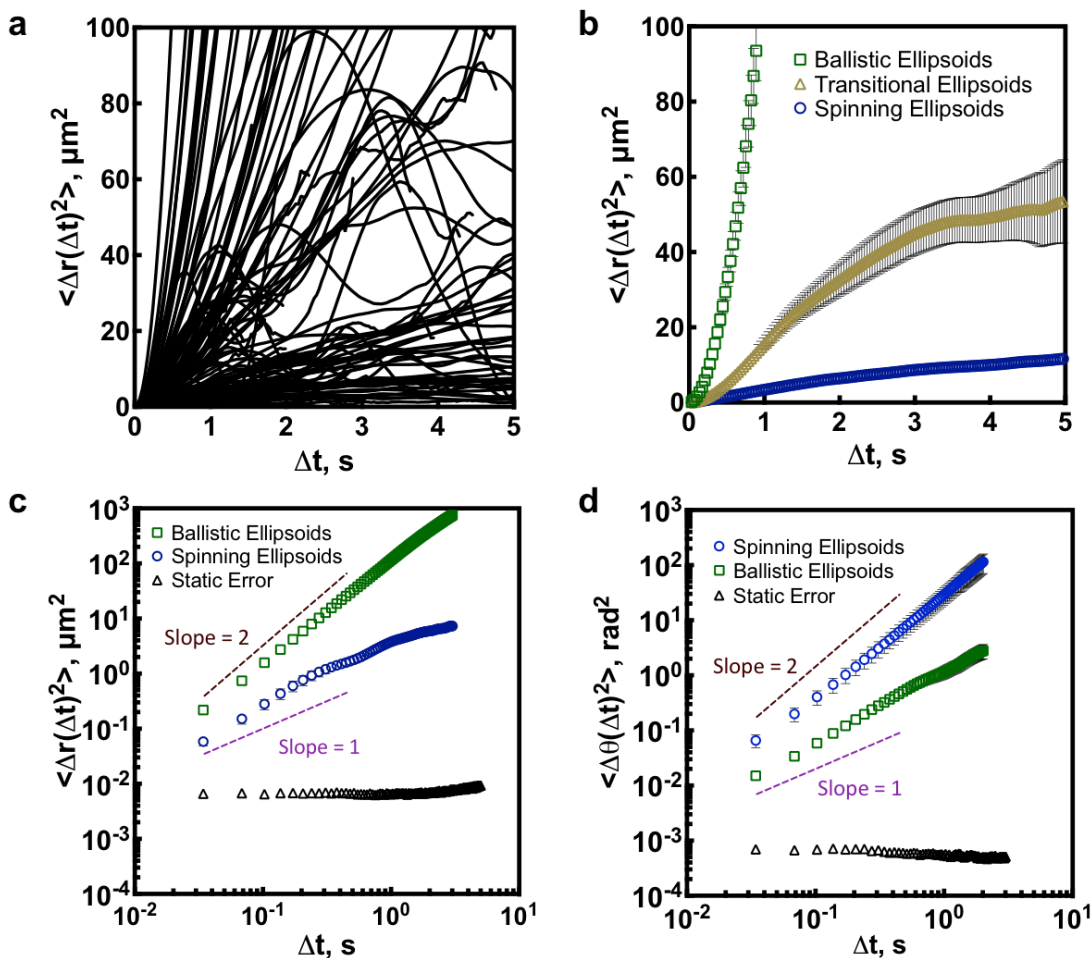


**Figure 3.7** Mobility of Janus ellipsoids ( $AR = 6.7 \pm 0.8$ ) in 8% hydrogen peroxide solution.

The linear MSD  $\langle \Delta r^2(\Delta t) \rangle$  of (a) all tracked particles and (b) selected particles for three identified types of mobility. A log-log plot of (c)  $\langle \Delta r^2(\Delta t) \rangle$  compares the translational motion and (d)  $\langle \Delta \theta^2(\Delta t) \rangle$  compares the rotational motion, of ballistic and spinning ellipsoids referencing a slope = 1. The error bars reflect an average of 5 particle trajectories.

Figure 3.7a shows the  $\langle \Delta r^2(\Delta t) \rangle$  of all particles tracked for ellipsoids of  $AR = 6.7 \pm 0.8$  in 8% hydrogen peroxide solution. The data demonstrate the wide range of observed displacement trajectories. The plot included ballistic ellipsoids exploring a large area at short time scales ( $< 1$  sec). There are other ellipsoids that are at times ballistic but also spin within the complete timespan the particle is tracked. These transitions from translation to rotation either occur spontaneously or

by particle collisions that affect the trajectory. Finally, spinning ellipsoids are observed with frequency comparable to ballistic ellipsoids; the centroids of these particles show minimal translational motion, even over very long periods ( $> 5$  sec). Figure 3.7b identifies the three observed trajectory types by averaging 5 trajectories in each group. The grouping shows that at short time scales, the translational motion of ballistic ellipsoids yields a rapidly increasing MSD. At long times, this class of active ellipsoids moves out of the imaged region. The MSD of the spinners is functionally different than the ballistic particles; the spinners show sublinear behavior of the MSD. These ellipsoids have a squared displacement at 5 seconds that is equivalent to what ballistic ellipsoids attain in less than 0.30 seconds. The MSD of transitional ellipsoids exhibits a combination of these ballistic and spinning features. For these particles, at short time scales ( $t < 1$  sec) the particle MSD is parabolic, as characteristic of ballistic motion, but at longer times, as spinning motion intermittently occurs, the displacement becomes variable. As these trajectories are clearly a mix of the two limiting cases of ballistic and spinning, we limit further analysis to the ballistics and spinning classes.

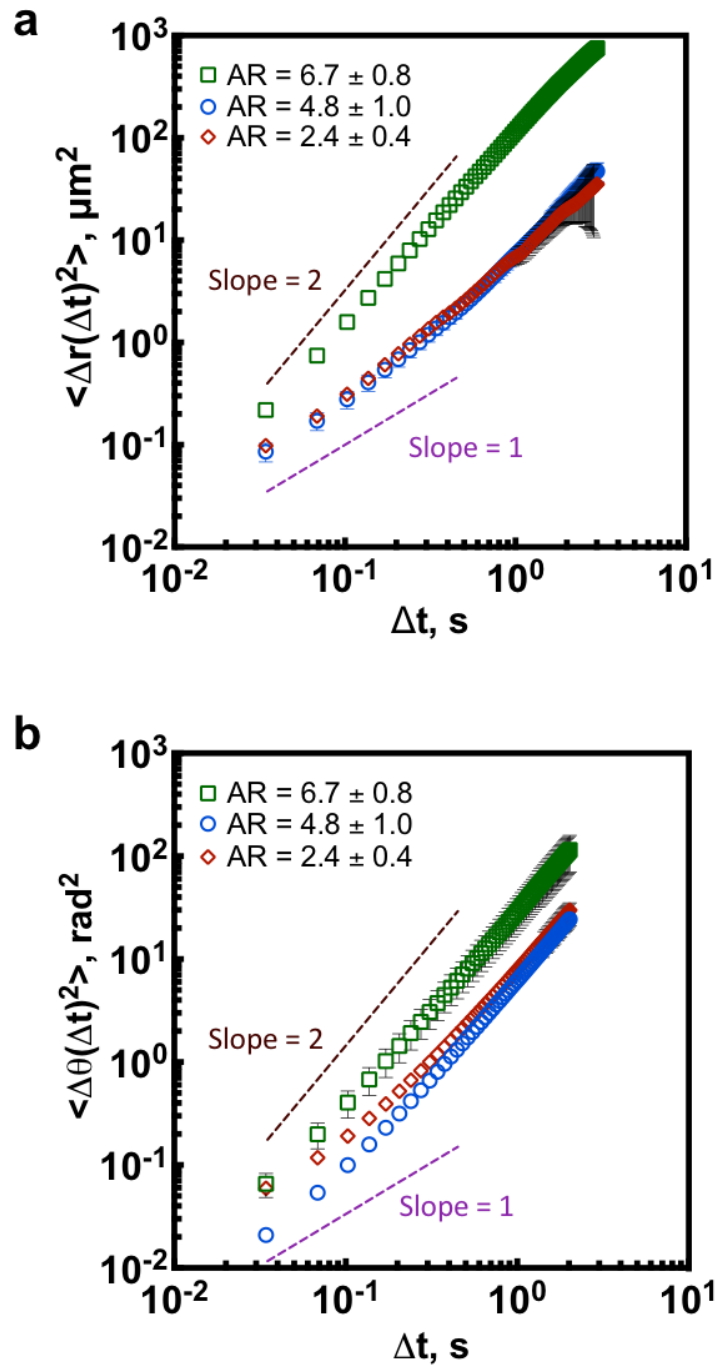


**Figure 3.8** Phoretic mobility of Janus ellipsoids with various aspect ratios in 8% peroxide solution.

(a) The MSD for ballistic particles and (b) the MSAD for spinning particles as function of particle aspect ratio. The error bars reflect an average of 5 particle trajectories.

Figure 3.8 shows the effect of reducing the ellipsoid aspect ratio from the previously studied case of 6.7. The ballistic displacements at aspect ratio 2.4 to 4.8, while still characteristic of active motion, are significantly less than the larger aspect ratio. In addition, the phoretic motion of ballistic particles at these two, smaller aspect ratios are roughly comparable. To further quantify the diffusive characteristics of these ellipsoids, we model the behavior for the different aspect ratios by fitting the results to the short time expression  $\langle \Delta r^2(\Delta t) \rangle = v^2 \Delta t^2 + 4D_T \Delta t$ , where  $D_T$  is the translational diffusion coefficient (computed as per Ref. 21) and  $v$  is the average velocity as determined from the data set. This equation is appropriate because the data are fit for times less than the time scale for rotational diffusion. These results are plotted in Table 3.1.

Turning to the spinning ellipsoids (Figure 3.8b), we see that all aspect ratios undergo large rotational trajectories. The power law slopes of the angular displacement of the three aspect ratios of 6.7, 4.8, and 2.4 are 1.9, 1.9, and 1.8 respectively. These slopes, much larger than unity, are consistent with sustained, rather than random, rotation of the ellipsoids. Thus, the spinning state of the ellipsoids is observed at multiple aspect ratio. The amount of rotation is furthermore aspect ratio dependent, with the aspect ratio 6.7 ellipsoids showing about 4 times more squared rotation than the lower aspect ratios.

We investigate the rotational diffusivity of the spinners using the MSAD relation and by fitting the data to  $\langle \Delta \vec{\theta}^2(\Delta t) \rangle = \omega^2 \Delta t^2 + 2D_R \Delta t$  as done by Ebbens et al<sup>22</sup>. We compute the rotational diffusion as per the expressions of Ref. 23. The angular velocity,  $\omega$ , is then determined from the measurements and reported in Table 3.1.

From the translational and angular velocities, we can calculate the force acting on ballistic ellipsoids and the torque acting on spinning ellipsoids, respectively. As the ellipsoids are observed to move sideways, the active force normal to the major axis is given by<sup>24</sup>:

$$F = 6\pi\mu a v C_1$$

where the viscosity  $\mu$ , and a geometric factor  $C_1$ , related to the ellipsoid eccentricity  $e = \sqrt{1 - b^2/a^2}$ , are used. The torque on the spinning ellipsoids is a function of  $\mu$ ,  $\omega$ , and is scaled by the major axis  $a$ , the minor axis  $b$ , and a geometric factor  $C_2$ , related to  $e$ :

$$T = 8\pi\mu a b^2 \omega C_2$$

with

$$C_1 = \frac{16}{3} e^3 \left[ 2e + (3e^2 - 1) \ln \frac{1+e}{1-e} \right]^{-1}$$

$$C_2 = \frac{4}{3} e^3 \left( \frac{2-e^2}{1-e^2} \right) \left[ -2e + (1+e^2) \ln \frac{1+e}{1-e} \right]^{-1}$$

The tabulated data for ellipsoids of the various aspect ratios and trajectory types is reported in Table 3.1.

**Table 3-1** Characteristics of active motion in ballistic and spinning ellipsoids as a function of aspect ratio in 8% hydrogen peroxide solution.

	Spheres (AR = 1)	AR = 2.4 ± 0.4	AR = 4.8 ± 1.0	AR = 6.7 ± 0.8
<i>Particle Descriptors</i>				
Pt surface area ( $\mu\text{m}^2$ )	1.6	2.0	2.1	2.2
$e$	-	0.91 ± 0.03	0.98 ± 0.01	0.99 ± 0.002
$C_1$	-	0.64	0.49	0.42
$C_2$	-	1.8	4.2	8.0
<i>Ballistic Ellipsoids</i>				
$D_T$ ( $\mu\text{m}^2/\text{s}$ ) – calc.	0.46	0.38	0.34	0.31
$v$ ( $\mu\text{m}/\text{s}$ ) – fit	2.2 ± 0.03	1.8 ± 0.009	1.9 ± 0.008	9.5 ± 0.04
$F$ ( $\text{kg} \cdot \mu\text{m}/\text{s}^2$ )	1.9e-8	2.5e-8 ± 4e-9	4.5e-8 ± 7e-9	2.5e-7 ± 2e-8
<i>Spinning Ellipsoids</i>				
$D_R$ ( $\text{rad}^2/\text{s}$ ) – calc.	-	1.3	0.49	3.3
$\omega$ ( $\text{rad}/\text{s}$ ) – fit	-	2.6 ± 0.0009	2.4 ± 0.009	5.3 ± 0.004
$T$ ( $\text{kg} \cdot \mu\text{m}^2 \cdot \text{rad}/\text{s}^2$ )	-	1.3e-7 ± 5e-8	2.4e-7 ± 1e-7	9.0e-7 ± 2e-7

We investigated the correlation of the results with other geometric descriptors of the particles. Table 1 shows that the amount of platinum coverage increases as aspect ratio is increased. The surface area of ellipsoids is greater than spheres by 22%, 27% and 31% for AR = 2.4, 4.8 and 6.7, respectively. This increased platinum coverage increases available catalyst activity. In terms of particle shape, there is a 7.4% difference in eccentricity from ellipsoids with AR = 2.4 to 4.8, but only a 1.0% difference from AR = 4.8 to 6.7.

The ballistic and spinning dynamics are comparable for AR = 2.4 and 4.8. However, for AR = 6.4 these dynamics are significantly enhanced relative to the lower aspect ratio particles. The translational velocities are comparable for spheres and ellipsoids with AR = 2.4 and 4.8, but is significantly higher for AR = 6.7. The accompanying active forces show an increasing trend as the aspect ratio is increased from spheres to ellipsoids. With the spinning ellipsoids, there is no significant difference in angular velocities between AR = 2.4 to 4.8; however, the angular velocity doubles for AR = 6.7 with  $5.3 \text{ rad/s}$ . The torque derived from these measurements shows a comparable trend.

### **3.5 Discussion**

Active Janus ellipsoids were observed moving sideways (relative to the ellipsoidal major axis) with the platinum coating on the particle oriented in the aft position. This relative orientation of the propulsion is a consequence of the platinum coverage along the hemispheroidal surface bounded by the major axis. The ellipsoids, apparently because of their anisotropy, can adopt multiple modes of active motion. We observed two cases of active motion – spinning and ballistic – with Janus ellipsoidal trajectories distributing between these two limits. In addition, the Langevin approach was applied to the ellipsoidal dynamics to characterize the active translational



and angular velocity, which enabled us to measure active force and torque for the ballistic and spinning ellipsoids.

While the translational displacement and active force of the ballistic trajectories is analogous to the well-studied case of Janus sphere propulsion, our characterization of propulsive torque for the class of spinning trajectories is new. Rotational motion of dimer and trimer particles has been previously observed<sup>6,22</sup>. The rotational motions were thought to be the consequence of the bounded spheres in clusters of particular orientations that frustrated the possibility of active spheres.

The data demonstrate that both ballistic and spinning ellipsoids experience translational and rotational motion, but with opposite time scale dependence. For ballistic ellipsoids, the time scale at which translational motion is observed dominates the rotation motion and for spinning ellipsoids the rotational motion overcomes translational motion. We observed transitions between these two states within the same trajectory; the transitions are either spontaneous or induced by interactions with surrounding particles. An interesting question to address in future work is the conditions that induced transitions, as well as the conditions for stability of these two different trajectory states.

There are two potential explanations for the observed complexity in the active particle trajectories. One possibility addresses the mechanism by which the Janus particles propel. As the peroxide is consumed to produce water and oxygen, there are two competing gradient profiles across the anisotropic particle. The concentration gradient of chemical products is depicted in Figure 3.5. There, the catalytic conversion of peroxide at the active platinum surface suggests that there is a higher concentration of products at the platinum cap than the polystyrene surface which is believed to drive the phoretic motion. However, there is the possibility of a concentration

gradient of the hydrogen peroxide across the particle as it is being consumed, with a higher peroxide concentration at the polystyrene surface than the platinum cap. This gradient profile would be shape dependent and become less pronounced with increased particle eccentricity. An improved streamline in working with ellipsoids with a significantly high aspect ratio is consistent with the marked ballistic motion observed with ellipsoids and not with spheres.

Secondly, if the diffusiophoretic gradient that drives the motion for these Janus colloids is combined with near-wall effects, then there is a potential for regimes in which the particle orientation is affected. For ballistic motion to occur, the particle orientation with respect to the substrate is likely symmetric due to a balance in competing concentration profiles and in other cases, the imbalance of the concentration gradient profile leads to spinning ellipsoids. This observation is critical because it suggests that the two states of the active motion of Janus ellipsoids are generated by long-lived, lubrication flows (one symmetric and one asymmetric relative to the minor axis of the particle), rather than the fixed conditions of the relative level of perfection/symmetry of the platinum coating. In addition, an imbalance of active motion as a result of particle collisions that cause a change translational and rotational motion, i.e: particles we classify as transitional, is excluded.

The active motion of Janus particles has been found by others to be dependent on particle size, shape, and platinum coating thickness. The present work adds anisotropy, particle eccentricity, and platinum surface area coverage, as additional determinants of propulsion and motion. In our study, there are clear effects of geometric characteristics on translational and rotational diffusivity, which yield a complex set of trajectory types that are distributed between the two limits of ballistic and spinning motion.

### 3.6 Conclusion

We have reported the dynamics of metallodielectric ellipsoids of colloidal polystyrene capped with platinum. We induced self-diffusiophoretic motion of prolate ellipsoids and established trajectory variability with monomeric colloids observing ballistic and spinning motions. Two-channel imaging confirmed the directional order of these complex trajectories. This analysis demonstrated the effect of varying the particle aspect ratio of the active Janus colloids. The highest aspect ratio dominated lower aspect ratios and Janus spheres in translational and rotational motion, regarding the MSD and MSAD. Using the Langevin approach, we fit models to our systems and concluded that active particles deviated from Brownian motion and moreover, MSD of prolate ellipsoids deviated from unity approximately twice more compared active spheres. Our observations therefore show that increasing the particle aspect ratio and catalytically active surface area, while conserving particle volume, can improve the particle velocity and augment the active force.

### 3.7 References

1. Walther, A.; Mu, A. H. E. Janus Particles. *Soft Matter* **2008**, *4*, 663–668.
2. Wu, L. Y.; Ross, B. M.; Hong, S.; Lee, L. P. Bioinspired Nanocorals with Decoupled Cellular Targeting and Sensing Functionality. *Small* **2010**, *6* (4), 503–507.
3. Hong, L.; Cacciuto, A.; Luijten, E.; Granick, S. Clusters of Charged Janus Spheres. *Nano Lett.* **2006**, *6* (11), 2510–2514.
4. Chen, Q.; Whitmer, J. K.; Jiang, S.; Bae, S. C.; Luijten, E.; Granick, S. Supracolloidal Reaction Kinetics of Janus Spheres. *Science* **2011**, *331* (6014), 199–202.
5. Howse, J.; Jones, R.; Ryan, A.; Gough, T.; Vafabakhsh, R.; Golestanian, R. Self-Motile Colloidal Particles: From Directed Propulsion to Random Walk. *Phys. Rev. Lett.* **2007**, *99* (4), 48102.
6. Gao, W.; Pei, A.; Feng, X.; Hennessy, C.; Wang, J. Organized Self-Assembly of Janus Micromotors with Hydrophobic Hemispheres. *J. Am. Chem. Soc.* **2013**, *135* (3), 998–

1001.

7. Paxton, W. F.; Kistler, K. C.; Olmeda, C. C.; Sen, A.; St. Angelo, S. K.; Cao, Y.; Mallouk, T. E.; Lammert, P. E.; Crespi, V. H. Catalytic Nanomotors: Autonomous Movement of Striped Nanorods. *J. Am. Chem. Soc.* **2004**, *126* (41), 13424–13431.
8. Jurado-Sánchez, B.; Sattayasamitsathit, S.; Gao, W.; Santos, L.; Fedorak, Y.; Singh, V. V.; Orozco, J.; Galarnyk, M.; Wang, J. Self-Propelled Activated Carbon Janus Micromotors for Efficient Water Purification. *Small* **2015**, *11* (4), 499–506.
9. Ke, H.; Ye, S.; Carroll, R. L.; Showalter, K. Motion Analysis of Self-Propelled Silica Particles in Hydrogen Peroxide Solutions. *J. Phys. Chem. A* **2010**, *114* (17), 5462–5467.
10. Anderson, J. L. Colloid Transport by Interfacial Forces. *Annu. Rev. Fluid Mech.* **1989**, *21* (1), 61–99.
11. Ebbens, S.; Tu, M. H.; Howse, J. R.; Golestanian, R. Size Dependence of the Propulsion Velocity for Catalytic Janus-Sphere Swimmers. *Phys. Rev. E - Stat. Nonlinear, Soft Matter Phys.* **2012**, *85* (2), 1–4.
12. Ebbens, S.; Gregory, D. A.; Dunderdale, G.; Howse, J. R.; Ibrahim, Y.; Liverpool, T. B.; Golestanian, R. Electrokinetic Effects in Catalytic Platinum-Insulator Janus Swimmers. *EPL (Europhysics Lett.)* **2014**, *106* (5), 58003.
13. Archer, R. J.; Campbell, A. I.; Ebbens, S. J. Glancing Angle Metal Evaporation Synthesis of Catalytic Swimming Janus Colloids with Well Defined Angular Velocity. *Soft Matter* **2015**, *11* (34), 6872–6880.
14. Koenig, S. H. Brownian Motion of an Ellipsoid: A Correction to Perrin's Results. *Biopolymers* **1975**, *14*, 2421–2423.
15. Han, Y.; Alsayed, A.; Nobili, M.; Yodh, A. G. Quasi-Two-Dimensional Diffusion of Single Ellipsoids: Aspect Ratio and Confinement Effects. *Phys. Rev. E - Stat. Nonlinear, Soft Matter Phys.* **2009**, *80* (1), 1–6.
16. Zheng, Z.; Han, Y. Self-Diffusion in Two-Dimensional Hard Ellipsoid Suspensions. **2010**, 1–10.
17. Champion, J. a; Katare, Y. K.; Mitragotri, S. Making Polymeric Micro- and Nanoparticles of Complex Shapes. *Proc. Natl. Acad. Sci. U. S. A.* **2007**, *104* (29), 11901–11904.
18. Shah, A. a.; Kang, H.; Kohlstedt, K. L.; Ahn, K. H.; Glotzer, S. C.; Monroe, C. W.; Solomon, M. J. Liquid Crystal Order in Colloidal Suspensions of Spheroidal Particles by Direct Current Electric Field Assembly. *Small* **2012**, *8* (10), 1551–1562.
19. Savin, T.; Doyle, P. S. Static and Dynamic Errors in Particle Tracking Microrheology. *Biophys. J.* **2005**, *88* (1), 623–638.

20. Tinevez, J.-Y. Simple Tracker Source Code. MATLAB 9.0 (R2016a) 2011.
21. Ken A. Dill, S. B. *Molecular Driving Forces: Statistical Thermodynamics in Chemistry and Biology*; Garland Science, 2003.
22. Ebbens, S.; Jones, R. A. L.; Ryan, A. J.; Golestanian, R.; Howse, J. R. Self-Assembled Autonomous Runners and Tumblers. *Phys. Rev. E - Stat. Nonlinear, Soft Matter Phys.* **2010**, *82* (1), 6–9.
23. Berg, H. C. *Random Walks in Biology*; Princeton University Press, 1993.
24. Bayly, P. V.; Lewis, B. L.; Ranz, E. C.; Okamoto, R. J.; Pless, R. B.; Dutcher, S. K. Propulsive Forces on the Flagellum during Locomotion of *Chlamydomonas Reinhardtii*. *Biophys. J.* **2011**, *100* (11), 2716–2725.

## CHAPTER 4

### Dense Packings of Colloidal Oblate Discoids

#### 4.1 Abstract

The use of anisotropic colloids is important in self-assembly, but there are challenges in achieving high packing densities comparable to theoretical estimates. Here we report the application of direct current electric field and light to suspensions of colloidal oblate spheroids (discoids) to achieve localized dense three-dimensional packings. High yields of oblate discoids, made possible by recent developments in fabrication techniques, are suspended in a refractive index and density-mismatched non-aqueous solvent. The suspensions are confined in a closed chamber electric field device with an indium-tin oxide coating at the electrodes. The voltage was varied from 1.65 – 2.2 V and a constant laser power of 370 W/m<sup>2</sup>. Experiments were also conducted at a fixed voltage of 1.95 V and varied laser power. Increasing the dc field voltage from 1.65 V to 1.95 V decreased the assembly time to reach terminal two-dimensional packing density of approximately 45% with dc alone. Applying dc and visible light concurrently led to a two-dimensional packing density of approximately 80% at an optimal condition of 1.95 V and 200 W/m<sup>2</sup>. Regions of two-dimensional hexagonal packing was also observed. We use confocal laser scanning microscopy to supply the light source, as well as image the experiments.

## 4.2 Introduction

Structural color from naturally occurring nano- and microstructures<sup>1-3</sup> has inspired fabricated three-dimensional crystalline assemblies in aims of achieving similar results in photonic devices. The building blocks of these biophotonic structures are often anisotropic in nature and fabricated assemblies are following suit in working with shape and multiphase anisotropic particles. The challenge of achieving high density packings with anisotropic particles, while limited by low yield from current fabrication techniques and increased orientational degree of freedom, is overcome by applying external fields. To achieve rapid ordering and a high packing density, on large scales, field-assisted methods such as alternating current (AC) electric fields<sup>4,5</sup>, direct current (DC) electric fields<sup>5-7</sup>, magnetic fields<sup>8,9</sup>, and light<sup>10</sup> have been used. These methods employ electrophoresis, thermophoresis, diffusiophoresis, and combinations thereof to densely pack colloidal particles.

One promising avenue in further maximizing packing fraction of colloidal particles is with working with ellipsoids. The increased shape anisotropy and surface curvature in ellipsoids relative to spheres is instrumental to their performance in applications such as improved near-wall particle flow<sup>11</sup> and adhesion<sup>12</sup>, achieving highly ordered structures for optical devices<sup>13</sup>, and use in consumer products<sup>14</sup>. In addition, aspherical ellipsoids are predicted to yield higher packing fractions than spheres in modeled ordered and disordered systems<sup>14-17</sup>. Disordered three-dimensional packings of oblate (discoids) and prolate (rods) spheroids are predicted to yield maximum packing density of between  $\phi = 0.70$  (as aspect ratio  $\sim 0.5$ ) and  $\phi = 0.72$  (at aspect ratio  $\sim 1.5$ )<sup>14</sup>, respectively. The random close packing limit for spheres is  $\phi = 0.64$  and for face-centered cubic packing is  $\phi = 0.74$ . Ordered assemblies of oblate and prolate spheroids pack to even greater densities of 0.77 and 0.75, respectively, at these aspect ratios<sup>15</sup>.

Here, we apply combinations of DC electric field and light to produce dense assemblies of discoids. DC electric field has previously been used for the electrophoretic deposition of spherical and rod-like colloids<sup>7</sup>. Likewise, by means of light-induced phoretic motion, colloidal spheres have been assembled into multilayer crystalline arrays<sup>10</sup>. In both methods, it is hypothesized that ion gradients are generated by the electrochemical reactions at the electrode surface and these ion gradients produce a field which drives the electrophoresis of the charged colloids. Colloids migrate toward the electrode surface, accumulating into dense structures. Maximum near-wall crystalline volume fractions of  $\phi = 0.47$ <sup>10</sup> for sphere assembly and  $\phi = 0.49$ <sup>18</sup> for prolate spheroids have been observed. These methods are favored because surface and materials may vary in these systems due to shape and interaction anisotropy, as long as the particle responds to the electric field induced by the electrochemically generated ion flow<sup>19</sup>.

## **4.3 Materials and Methods**

### **4.3.1 Janus Discoid Synthesis**

Biaxial straining of spheres to produce discoids have been fabricated by others<sup>20,21</sup>, but adaptations are introduced. To synthesize high yields of discoids, 600 mL of a 2.0 vol % solution of carboxylate-modified polystyrene spheres (PS) (1.9  $\mu\text{m}$ , Life Technologies) is added to 20 ml of 10% (w/v) Poly(vinyl alcohol) (PVA) (MW = 30,000-70,000, Sigma-Aldrich) in water solution. The solution is well-mixed before pouring in an OmniTray (Nunc OmniTray, Thermo Scientific) and allowed to dry for 48 hrs at room temperature. Once dried, the film is cut into (4) 1.25 in. diameter films, each placed in between two solid silicone rubber sheets (0.010" Thick - 20a Durometer Hardness, Marian Chicago) and assembled in a Carver Press as shown in Figure 4.1a. To allow for contact between the film and press, an initial pressure of 1,500  $\text{lb}_f$  is applied. The



film is heated to 120°C for 1.5 hrs at this pressure. Next, the pressure is increased to 20,000 lb<sub>f</sub> and kept at 120°C for 10 mins. The sample is allowed to cool to room temperature while under pressure.

The pressed film ( $\Delta r/r = 0.24 \pm 0.03$ ) is removed from the press, suspended in DI water, and sonicated in a bath sonicator (Branson Ultrasonics) for 1.5 hrs. The DI water is then exchanged five times using centrifugation to remove the PVA from the particle suspension (Sorvall Legend X1R, 5,000 G for 15 min). The discoids are solvent-exchanged with 0.1mM tetrabutylammonium chloride (TBAC) in dimethyl sulphoxide (DMSO) three times using centrifugation (Eppendorf MiniSpin Plus, 10,000 rpm for 10 min). The colloidal particles are refractive and density mismatched with the solvent. The result of the syntheses of polystyrene disks is shown in Figure 4.1b.

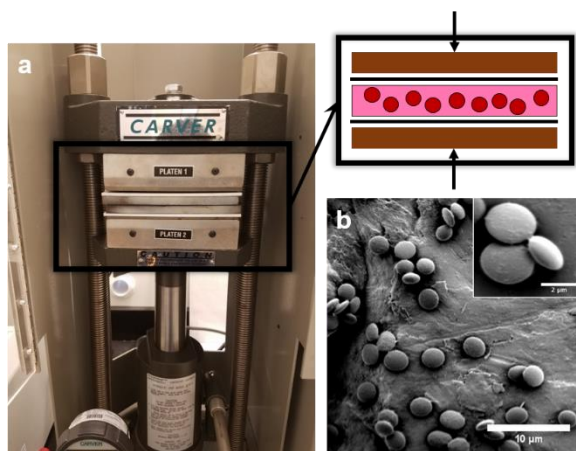


**Figure 4.1** *Fabrication technique and micrographs of PS discoids.*

(a) A heated Carver press is used to achieve biaxial strain of PS embedded films. (2) SEM image of polystyrene disks with measured semi-axis dimensions:  $a = 1.4 \pm 0.1 \mu\text{m}$ ,  $b = 1.2 \pm 0.1 \mu\text{m}$ ,  $c = 0.6 \pm 0.1 \mu\text{m}$ . Scale bar is 2  $\mu\text{m}$ .

The biaxial stretching yields triaxial discoids (Figure 4.1b) with semi-axis dimensions  $a = 1.4 \pm 0.1 \mu\text{m}$ ,  $b = 1.2 \pm 0.1 \mu\text{m}$ ,  $c = 0.6 \pm 0.1 \mu\text{m}$ . The deviation from ideal oblate

ellipsoids, in comparing the equatorial axes, is  $\Delta r/r \sim 0.15 \pm 0.12$ . The particles are within 20% of perfectly symmetric discoids with an average equatorial axis,  $1.3 \pm 0.2 \mu\text{m}$ , along with the polar axis,  $0.6 \pm 0.1 \mu\text{m}$ , yields an approximate particle aspect ratio,  $r_p \sim 0.45 \pm 0.17$ .

#### **4.3.2 Sample Preparation for Field-Induced Assembly**

The DC electric field device used to assemble the polystyrene disks is described by Shah et al<sup>7</sup>. Briefly, approximately 15  $\mu\text{l}$  of colloidal disk suspension at an initial volume fraction of  $1.9 \pm 0.2 \%$  is dispensed into a chamber with a cylindrical geometry (ID = 4.5 mm, H = 1.0 mm). ITO-coated microscope coverslips (ZC & R Coatings, Inc.) were used as the top and bottom surface of the chamber, with the surface with the ITO coating facing inwards. Non-adhesive silicone isolators (JTR12R-1.0, Grace Bio-Labs) were used as boundaries for the cylindrical chamber. Prior to the assembly of the device, the ITO-coated microscope coverslips are treated in a photosensitized oxidative chamber (Jelight UVO Cleaner) for 5 min, wiped with isopropanol, then dried under forced air for 1-2 min. The self-assembly of the ellipsoids is observed by confocal microscopy (CLSM, Nikon A1R).

#### **4.3.3 Confocal Laser Scanning Microscopy**

CLSM time series image volumes were acquired using a Nikon A1R CLSM instrument (100 $\times$ , 1.4 NA, oil immersion objective lens). The fluorescent polystyrene is imaged with a 561 nm excitation with emission collected over the range 570 to 620 nm. XY images of 512 x 512 pixels with a spatial resolution of 0.062  $\mu\text{m}/\text{pixel}$  were collected at 15 fps. Once three-dimensional assembly was observed, XY images were collected at various axial heights with the sample. The separation between the slices at different axial heights was 0.062  $\mu\text{m}$ . Typically, about 160 images in the z direction were collected, scanning 10  $\mu\text{m}$  in depth within the sample.

## 4.4 Results

### 4.4.1 Kinetics of field-induced assembly

PS discoids dispersed in a non-aqueous solvent of 0.1Mm TBAC in DMSO were subjected to an applied dc voltage. A  $\sim 30 \times 30 \mu\text{m}$  region was imaged at the ITO coverslip as dc voltages ranged from 1.65V to 2.2V. Figure 4.2 shows that accumulation of the discoids was a function of the voltage applied. The 2D accumulation time was on the order of minutes ( $< 20$  mins). Due to the degree of freedom of the discoids, there are regions of inconsistent particle alignment in the observed packed assemblies.

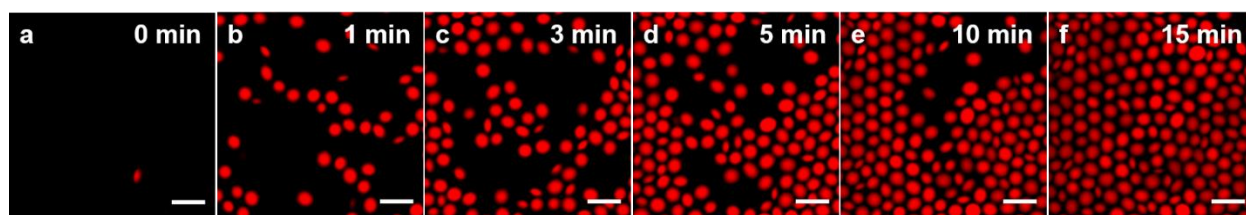


**Figure 4.2** Representative 2D confocal images of PS discoids in 0.1Mm TBAC in DMSO under applied dc voltage.

Time lapse images of discoid assembly near the coverslip under applied dc voltage of 1.95V. All scale bars are  $5 \mu\text{m}$ .

To further effect the assembly process, visible light was applied simultaneously with various dc voltages. The light source was supplied by a 405 nm laser light and turned on for the entire duration of the experimental study. The characteristic time at which 2D assembly occurred was dependent on voltage intensity and was further augmented with visible light (Figure 4.3). As the applied dc field strength is increased, the concentration time is decreased as the system reaches a steady state. The PS discoids also begin to concentrate near the coverslip as well as predominantly orient themselves laterally as evidence by the confocal images. Increasing the

voltage applied from 1.85 to 1.95 V decreases the accumulation time for particles to move to the coverslip. The maximum 2D packing density achieved with the dc field alone at 1.95 V was approximately 45%. Adding visible light with a laser power of  $370 \text{ W/m}^2$  at voltages of 1.65 V, 1.75 V and 1.95 V achieved a faster accumulation time but negatively affected particle stability and orientation as shown by the oscillating packing trend in Figure 4.3. The  $1.75 \text{ V} + 370 \text{ W/m}^2$  condition achieved faster assembly than  $1.65 \text{ V} + 370 \text{ W/m}^2$ , which is consistent with the dc field trend of higher voltages leading to improved timescale of phoretic motion. At  $1.95 \text{ V} + 370 \text{ W/m}^2$  the laser power proved to be too strong and yield particle-substrate instability and inconsistent particle alignment. Upon lowering the laser power, an optimal condition of  $1.95 \text{ V} + 200 \text{ W/m}^2$  yielded to a two-dimensional packing density of approximately 80%.

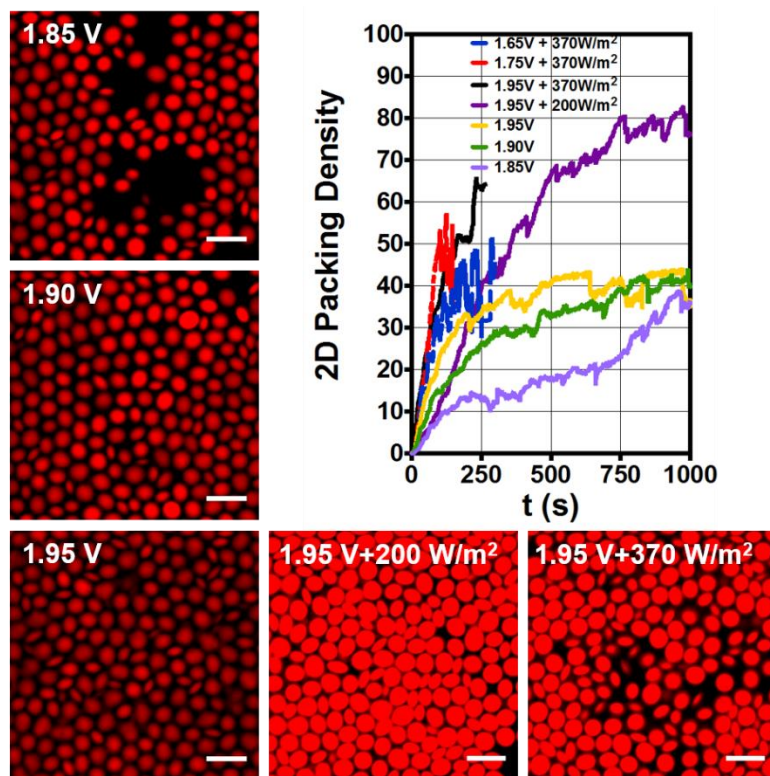


**Figure 4.3** Kinetics of assembly under applied dc voltage and visible light.

2D packing density increases until it reaches steady stage for PS discoids under applied dc voltage (1.65V – 1.95V) and visible light (200 W/m<sup>2</sup> and 370 W/m<sup>2</sup>). Representative 2D confocal micrographs show PS discoids near the coverslip for 1.85V – 1.95V, 1.95V + 200 W/m<sup>2</sup>, and 1.95V + 370 W/m<sup>2</sup>. All scale bars are 5 µm.

#### 4.4.2 Packing structure of PS discoids

To establish the phase behavior of dc field induced assembly of isotropic particles, we assemble a suspension of 2 µm spheres with an applied 2.2V field strength. The sphere packing structure is then compared to the discoid packing structure under the same field condition (Figure 4.4). Comparing the 2D packing of the isotropic spheres and discoids we see that the shape anisotropy has a significant effect on phase behavior. The crystalline spheres show spatial order and isotropic inter-particle interaction with its nearest neighbors. The discoids possess an increased degree of freedom due to shape anisotropy and as such, shows limited spatial order and regions at

which particles orient in various fashions. This incongruity in packing is observed more as layers above the coverslip and within the assembly are imaged (Figure 4.4c-d). The dc field-induced effect yields 3-4 layers of the accumulated colloidal structures for the discoids. The isotropic spheres presented a quasi-2D colloidal crystal and the discoids were densely packed but disordered.

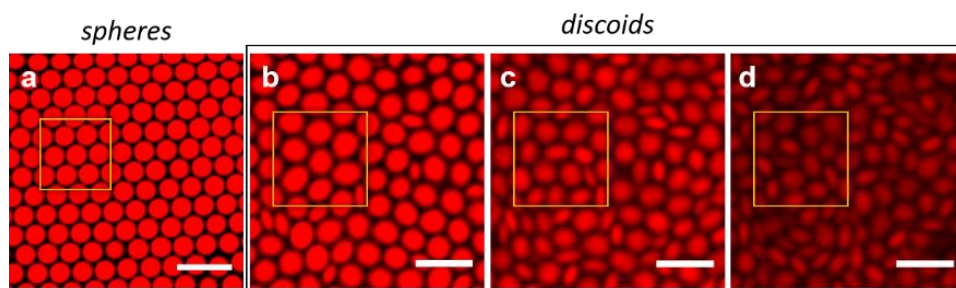


**Figure 4.4** 2D packing structures of PS colloids in 0.1Mm TBAC in DMSO under applied 2.2V.

The 2D packing structure of (a) 2  $\mu\text{m}$  PS spheres compared an assembly of PS discoids in three distinct layers from closest to the substrate to  $\sim 5 \mu\text{m}$  within the sample, showing (b) layer 1, (c) layer 2 and (d) layer 3. All scale bars are 5  $\mu\text{m}$ .

## 4.5 Discussion

The regions of 2D hexagonal ordering observed under the different external field conditions showed promise in being able to experimentally achieve ordered packing of colloidal discoids. There were several contributing factors for the packing structures observed with the oblate discoids. As mentioned earlier, the fabrication process yields triaxial oblate ellipsoids and therefore adds a third dimension of shape anisotropy that affects the phase behavior of the discoids in assemblies. The refractive-index and density mismatched colloidal system of polystyrene in DMSO meant the system could be optimized in future observations of dynamic changes. The kinetic effect of applied external field was similar to what has been observed by others<sup>10,18</sup>. In considering the first assembled layer, the 2D packing density for the applied field experiments

reached ~45% at 1.95V and ~50% at 1.75V + 370W/m<sup>2</sup>. There was an observed particle instability with the application of visible light. Most particles became affixed to the ITO surface on approach, while others continually re-oriented while near the surface. This dynamic change in 2D surface coverage is captured in the fluctuating packing density as the system approaches steady state (Figure 4.3) for the combinatory field systems. By decreasing the laser intensity from 300 W/m<sup>2</sup> to 200 W/m<sup>2</sup> at 1.95V, the particle instability was abated and resulted in a 2D packing density of ~80%. The two dimensional square lattice packing of circles has a packing fraction of  $\phi = 0.785$ , while the maximum planar packing density of circles is of a hexagonal lattice at  $\phi = 0.907^{22}$ . Therefore, the assembled discoids were able to achieve a higher 2D packing density than the square lattice packing of circles and there are indications of a preferred hexagonal packing lattice with discoid in the assembled regions shown in Figure 4.4.

The novelty of introducing discoids led to complex dynamic challenges that differs from previous studies with anisotropic constituents. While 2D ordering was observed with some defects, the discoids were consistently observed to favor disorder in their 3D assemblies. This was this case for dc only experiments and when both dc and visible light were applied. However, Figure 4.3 and 4.4 shows that the discoids can be ordered and aligned with the application of external fields. In addition, in regions with a highly ordered hexagonal lattice in the first layer, the second layer was also hexagonally packed with a slight angular offset in layering (Figure 4.4b-c).

## 4.6 Conclusion

We induce the colloidal assembly of oblate discoids by using dc electric field and light to generate a gradient field which drives the electrophoresis of the charged colloids. The packing of discoids was dependent of voltage and power of visible light. The assemblies achieved showed

promise in achieving ordered 2D structures, however, the 3D structures were disordered under the conditions tested. Varying the voltage showed no significant effect on promoting ordered 2D crystalline structures void of packing defects but it remains an efficient method for rapid accumulation. Furthermore, the use of visible light increased the characteristic packing time and packing fraction. The maximum stable 2D packing density achieved with the dc field alone was approximately 45%. Of the dc field and visible light combinations tested, the maximum 2D density was approximately 80%. By combining dc voltage and visible light we were able to approach significantly higher packing density comparable to the maximum planar hexagonal lattice packing of circles. In addition, the application of external field showed for the first assembled layer, the discoids favored hexagonal packing.

#### 4.7 References

1. Saranathan, V.; Osuji, C. O.; Mochrie, S. G. J.; Noh, H.; Narayanan, S.; Sandy, A.; Dufresne, E. R.; Prum, R. O. Structure, Function, and Self-Assembly of Single Network Gyroid (I4132) Photonic Crystals in Butterfly Wing Scales. *Proc. Natl. Acad. Sci.* **2010**, *107* (26), 11676–11681.
2. Vukusic, P.; Sambles, J. R. Photonic Structures in Biology. *Nature* **2003**, *424* (6950), 852–855.
3. Dufresne, E. R.; Noh, H.; Saranathan, V.; Mochrie, S. G. J.; Cao, H.; Prum, R. O. Self-Assembly of Amorphous Biophotonic Nanostructures by Phase Separation. *Soft Matter* **2009**, *5* (9), 1792.
4. Gangwal, S.; Cayre, O. J.; Velez, O. D. Dielectrophoretic Assembly of Metallodielectric Janus Particles in AC Electric Fields. *Langmuir* **2008**, *24* (23), 13312–13320.
5. Trau, M.; Saville, D. A.; Aksay, A. Field-Induced Layering of Colloidal Crystals. *Sci. New Ser.* **1996**, *272* (5262), 706–709.
6. Rogach, A. L.; Kotov, N. A.; Koktysh, D. S.; Ostrander, J. W.; Ragoisha, G. A. Electrophoretic Deposition of Latex-Based 3D Colloidal Photonic Crystals : A Technique for Rapid Production of High-Quality Opals. *Chem. Mater.* **2000**, No. 16, 2721–2726.
7. Shah, A. a; Ganesan, M.; Jocz, J.; Solomon, M. J. Direct Current Electric Field Assembly



- of Colloidal Crystals Displaying Reversible Structural Color. *ACS Nano* **2014**, 8 (8), 8095–8103.
8. Ahniyaz, A.; Sakamoto, Y.; Bergström, L. Magnetic Field-Induced Assembly of Oriented Superlattices from Maghemite Nanocubes. *Proc. Natl. Acad. Sci. U. S. A.* **2007**, 104 (45), 17570–17574.
  9. Ding, T.; Song, K.; Clays, K.; Tung, C. H. Fabrication of 3D Photonic Crystals of Ellipsoids: Convective Self-Assembly in Magnetic Field. *Adv. Mater.* **2009**, 21 (19), 1936–1940.
  10. Kim, Y.; Shah, A. A.; Solomon, M. J. Spatially and Temporally Reconfigurable Assembly of Colloidal Crystals. *Nat. Commun.* **2014**, 5, 1–8.
  11. Gavze, E.; Shapiro, M. Particles in a Shear Flow near a Solid Wall: Effect of Nonsphericity on Forces and Velocities. *Int. J. Multiph. Flow* **1997**, 23 (1), 155–182.
  12. Lee, S. Y.; Ferrari, M.; Decuzzi, P. Design of Bio-Mimetic Particles with Enhanced Vascular Interaction. *J. Biomech.* **2009**, 42 (12), 1885–1890.
  13. Kim, S.-H.; Lee, S. Y.; Yang, S.-M.; Yi, G.-R. Self-Assembled Colloidal Structures for Photonics. *NPG Asia Mater.* **2011**, 3 (1), 25–33.
  14. Donev, A.; Cisse, I.; Sachs, D.; Variano, E. A.; Frank, H.; Connelly, R.; Torquato, S.; Chaikin, P. M. Improving the Density of Jammed Disordered Packings Using Ellipsoids. *Science (80-. )*. **2004**, 303 (5660), 990–993.
  15. Donev, A.; Stillinger, F. H.; Chaikin, P. M.; Torquato, S. Unusually Dense Crystal Packings of Ellipsoids. *Phys. Rev. Lett.* **2004**, 92 (25), 255506–1.
  16. Delaney, G.; Weaire, D.; Hutzler \*, S.; Murphy, S. Random Packing of Elliptical Disks. *Philos. Mag. Lett.* **2005**, 85 (2), 89–96.
  17. Delaney, G. W.; Cleary, P. W. The Packing Properties of Superellipsoids. *EPL (Europhysics Lett.)* **2010**, 89 (3), 34002.
  18. Shah, A. a.; Kang, H.; Kohlstedt, K. L.; Ahn, K. H.; Glotzer, S. C.; Monroe, C. W.; Solomon, M. J. Liquid Crystal Order in Colloidal Suspensions of Spheroidal Particles by Direct Current Electric Field Assembly. *Small* **2012**, 8 (10), 1551–1562.
  19. Glotzer, S. C.; Solomon, M. J. Anisotropy of Building Blocks and Their Assembly into Complex Structures. *Nat. Mater.* **2007**, 6 (8), 557–562.
  20. Hsiao, L. C.; Schultz, B. A.; Glaser, J.; Engel, M.; Szakasits, M. E.; Glotzer, S. C.; Solomon, M. J. Metastable Orientational Order of Colloidal Discoids. *Nat. Commun.* **2015**, 6, 8507.
  21. Ahn, S. J.; Ahn, K. H.; Lee, S. J. Film Squeezing Process for Generating Oblate

Spheroidal Particles with High Yield and Uniform Sizes. *Colloid Polym. Sci.* **2016**, 294 (5), 859–867.

22. Fukshansky, L. Revisiting the Hexagonal Lattice: On Optimal Lattice Circle Packing. *Elem. der Math.* **2011**, 66 (1), 1–9.

## CHAPTER 5

### Conclusions and Future Work

#### 5.1 Concluding Remarks

The objective of this dissertation was to show that identifying of the relative contributions of characteristic features in anisotropic colloidal particles improves the (i) scope of designing new and optimized constituents in dynamic systems, (ii) understanding inter-particle and particle-solvent interactions, and (iii) influences the phase behavior in steady-state and equilibrium conditions. We employed sophisticated fabrication techniques, high-resolution imaging, and theoretically modelling provide evidence of anisotropic effects on self-assembly and self-propulsion on a colloidal scale. Early on, we show that the thickness of the metallic phase was correlated to preferentially binding and cluster growth with PS-Au Janus spheres. The systematic probe of phase anisotropy was then extended to manipulating particle shape. The marriage of colloidal ellipsoids and catalytic metal hemispheres led to ballistic and rotationally active monomeric colloids with PS-Pt prolate ellipsoids. The complex trajectories had only previously been reported with clusters of Janus of spheres creating an orientational imbalance. Realizing the dynamic potential of ellipsoids with particle-solvent interactions compelled the investigation of interparticle interactions and phase behavior in Chapter 4.

In Chapter 2, we studied the contributions of kinetics, salt concentration, SAM hydrophobicity and chain length, and metallic layer thickness (between 10 and 40 nm) on the

cluster probability distributions of Janus spheres comprised of polystyrene and gold. This analysis demonstrated the effect of the surface chemistry of the Janus colloids on self-assembly and clustering. The results of self-assembly are independent of the different SAM chemistries tested but strongly linked with the thickness of the Au layer on the Janus particle. Theoretical modeling of the separation dependent Hamaker constant support an effect of Au thickness on attractions in the system, proving that metallic layer thickness is more influential than hydrophobic interactions in determining the inter-particle preferential binding and affinity.

In Chapter 3, we showed the complex trajectories of prolate Janus ellipsoids. PS spheres were elongated and half-coated with platinum. Using hydrogen peroxide as a chemical fuel, we induced monomeric diffusiophoretic motion of the Janus ellipsoids in aqueous suspensions. There were complex trajectories of spinning and ballistic motions. These trajectories were analyzed against model systems and found to be more active than Janus spheres of comparable particle volume. In addition, we quantify the active force and torque generated. The enhanced activity while conserving particle volume was surprising consider the orientation of the Janus balance across the ellipsoid. We proposed that the concentration gradient profile was affected by the particle's reconditioned proximity to the coverslip to its shape led to significantly higher MSD than what we observed with Janus spheres.

Chapter 4 describes the outcome of oblate discoids subjected to external fields of dc voltage and visible light. The application of dc voltage particles rapidly packed near the coverslip. Concurrent application of dc voltage and visible light resulted in increased electrophoretic sedimentation compared to when with only dc fields. Both dc field and dc field + visible light conditions resulted in some 2D ordering. However, there were particle orientation defects that did not yield and propagated within observed 3D structures.

## **5.2 Future work**

Our understanding of shape and surface anisotropy as it influences inter-particle and particle-solvent interactions is continually expounded. In this dissertation, we showed that the ability to design and isolate the anisotropy of colloidal materials combined with direct visualization and modelling techniques, have improved upon the scientific record. Here, we propose specific pathways to expand upon this work corollary to the results presented in this dissertation.

### **Intersection of particle aspect ratio and size of chemically-induced propulsive systems**

The translational and rotational motion of Janus ellipsoids was shown to be different from Janus spheres of comparable particle volume in Chapter 3. However, the incremental change in active motion as particle aspect ratio increased is not immediately obvious. There are many physical characteristics that inform ellipsoidal shape and thereby active motion of its Janus state. It is clear that ellipsoids pose unique behavioral circumstances with regard to near-wall particle flow<sup>1</sup>. Therefore, particle variety is needed in exploring these physical characteristics and providing a quantitative answer as to why and how ellipsoids yield more active and complex trajectories. The effect of aspect ratio at fixed particle volume and fixed aspect ratio at various particle volumes would need to be evaluated to expand the scope of correlation to complex trajectories.

### **Ordered discolid assemblies and optical properties.**

In Chapter 4, shape anisotropy was explored largely in part to report packing densities. However, ordered assemblies of ellipsoids have the potential for novel optical properties. Additional experiments can be performed to (1) improve discolid symmetry during fabrication, (2) determine external field parameters that yield ordered 3D crystalline structures, and (3) determine

the optical properties of 3D ordered assemblies of discoids. Can larger quantities of discoids be fabricated without sacrificing homogeneity? Thus far, compression and elongation technique have been the most promising options<sup>2-4</sup>, of which I employed for my experiments. With the application of external field, the shape and size of the particle has been shown to influence assemble and ordering and those principles apply to discoids. Lastly, the ability to compare diffraction of ordered discoids to equivalent systems consisting of isotropic spheres<sup>5</sup> would provide insight into the enhancement of photonic devices with shape anisotropic components.

### 5.3 References

1. Gavze, E.; Shapiro, M. Particles in a Shear Flow near a Solid Wall: Effect of Nonsphericity on Forces and Velocities. *Int. J. Multiph. Flow* **1997**, *23* (1), 155–182.
2. Champion, J. a; Katare, Y. K.; Mitragotri, S. Making Polymeric Micro- and Nanoparticles of Complex Shapes. *Proc. Natl. Acad. Sci. U. S. A.* **2007**, *104* (29), 11901–11904.
3. Hsiao, L. C.; Schultz, B. A.; Glaser, J.; Engel, M.; Szakasits, M. E.; Glotzer, S. C.; Solomon, M. J. Metastable Orientational Order of Colloidal Discoids. *Nat. Commun.* **2015**, *6*, 8507.
4. Ahn, S. J.; Ahn, K. H.; Lee, S. J. Film Squeezing Process for Generating Oblate Spheroidal Particles with High Yield and Uniform Sizes. *Colloid Polym. Sci.* **2016**, *294* (5), 859–867.
5. Shah, A. a.; Kang, H.; Kohlstedt, K. L.; Ahn, K. H.; Glotzer, S. C.; Monroe, C. W.; Solomon, M. J. Liquid Crystal Order in Colloidal Suspensions of Spheroidal Particles by Direct Current Electric Field Assembly. *Small* **2012**, *8* (10), 1551–1562.

## APPENDIX

### Appendix A

#### Particle characteristics and additional analysis for salt-induced self-assembly systems

##### A.1 Contact angle measurements.

By means of contact angle measurements, we evaluate the hydrophobicity of uncoated carboxylate-modified polystyrene spheres and gold coatings functionalized with OT, MOA, or MHDA, relative to the control of no thiol (SAM) functionalization. The gold coatings were evaluated in two ways: one with planar coatings on a microscope slide and the other with a monolayer of unmodified and thiol-modified gold-coated Janus spheres. Figure Appendix A.1 shows the behavior of a water droplet on the different surfaces. The equilibrium contact angle,  $\theta$ , was measured from the images by the method shown in red in Figure Appendix A.1. The progression of wettability among these planar layers of thiol-functionalized gold is consistent with the sequence of hydrophobicity reported using a monolayer of Janus spheres, as reported in Table Appendix A.1.

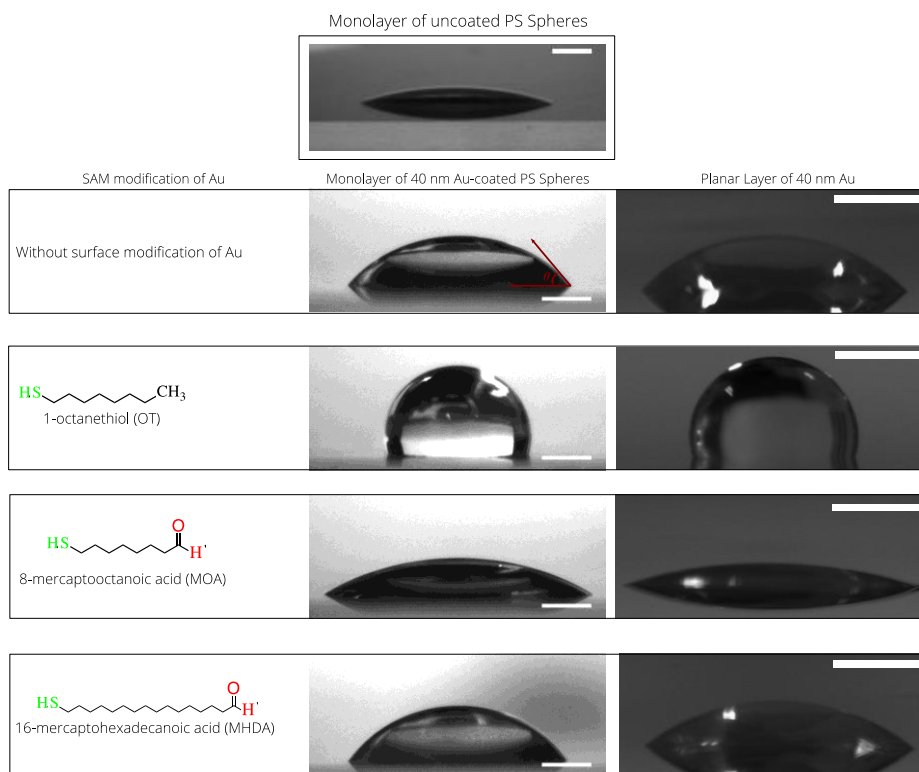


**Figure Appendix A.1 Wettability of a layer of varied surfaces.**

Substrate of uncoated polystyrene spheres and planar layer of 40 nm gold compared with a monolayer of Janus spheres with 40 nm gold coatings with no SAM functionalization, OT, MOA, and MHDA. All scale bars are 1 mm. This figure was originally published in [Shemi, O.; Solomon, M. J. *Langmuir* **2014**, *30*, 15408–15415].

**Table Appendix A.1 Contact angles of a monolayer of various surfaces were measured.** This table was originally published in [Shemi, O.; Solomon, M. J. *Langmuir* 2014, *30*, 15408–15415].

Uncoated carboxylate-modified PS				
Monolayer, $\theta/^\circ$	19 $\pm$ 3			
	Au	Au-OT	Au-MOA	Au-MHDA
Janus Monolayer, $\theta/^\circ$	42 $\pm$ 2	115 $\pm$ 7	26 $\pm$ 2	50 $\pm$ 2
Planar Layer, $\theta/^\circ$	43 $\pm$ 2	103 $\pm$ 4	15 $\pm$ 1	37 $\pm$ 1



## A.2 Cluster Analysis.

As each 512 pixel x 128 pixel image is taken of each individual channel (forming a composite image) at incremental depths within the total image volume, the different clusters come slightly in and out of focus as they undergo Brownian motion, thereby revealing their cluster size and configuration (Figure Appendix A.2a). We counted the number of particles in a cluster and confirmed their geometry by viewing image frames of each individual channel, as well as the composite images, of a stack recording (Figure Appendix A.2b). This inspection allowed us to quantify the population of a particular cluster size across three independent CLSM image volumes for any given experimental condition.

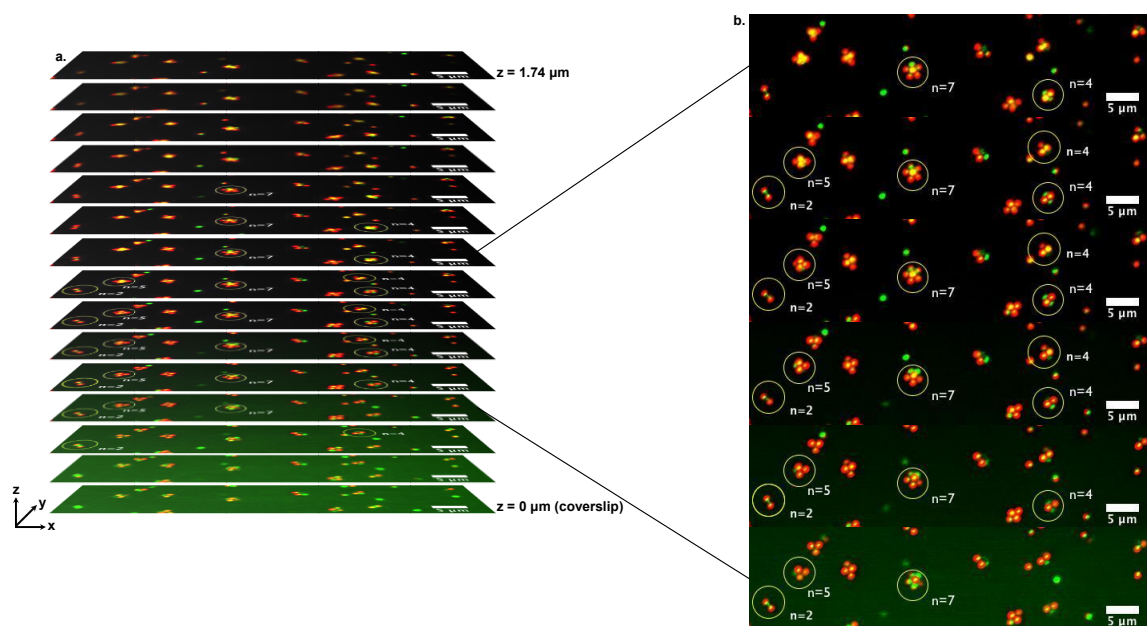


**Figure Appendix A.2** CLSM images of assembled Janus particles showing cluster identification method.

(a) 512 X 128 pixel images taken at various focal planes within a sample. (b) Select frames within an image volume confirming various cluster geometries as they appear in and out of focus. All scale bars are 5  $\mu\text{m}$ . This figure was originally published in [Shemi, O.; Solomon, M. J. *Langmuir* **2014**, *30*, 15408–15415].

### A.3 Effect of salt concentration on cluster size distribution.

The effect of four different salt concentrations – 1 mM, 2 mM, 2.5 mM, and 3 mM – on the cluster probability distribution was studied for unmodified, OT-modified, and MHDA-modified Au (40 nm)-PS Janus spheres in addition to MOA-modified Janus spheres already presented in Figure 2.5. Figure Appendix A.3 shows a salt concentration comparison for these Janus spheres of varied surface chemistry. Using unmodified PS-Au Janus spheres, no clusters form at 1 mM. Similar amounts of clusters with  $n = 1$ ,  $n = 4$  and  $n = 7$  spheres were induced at 2 mM. At 2.5 mM, the most abundant cluster size is  $n = 4$  and at 3 mM, this value shifts to  $n = 6$ . With hydrophobic OT-modified particles, in a 2 mM NaCl suspension a variety of cluster sizes were observed with specific Au-to-Au binding. The suspension comprised of predominantly individual Janus spheres and the largest cluster size observed were assemblies of  $n = 6$  spheres. There was no significant variation in the cluster probability distribution from 2 mM to 2.5 mM. For the 3 mM suspension, approximately 50% of the suspension was assembled into clusters of  $n = 7$  spheres. With hydrophilic MHDA-modified Janus spheres trend of producing larger clusters as NaCl is increased remains. Lastly, as in the main text, MOA-modified Janus spheres in a 2 mM suspension were present predominantly as individual Janus spheres. At 2.5 mM, there is a slight decrease in the abundance of individual spheres. The cluster distributions are similar to the 2 mM condition. At 3 mM NaCl, approximately 40% of the suspension was assemblies of  $n = 7$  spheres, ~25% of  $n = 6$ , and minimal amounts of the other cluster sizes.

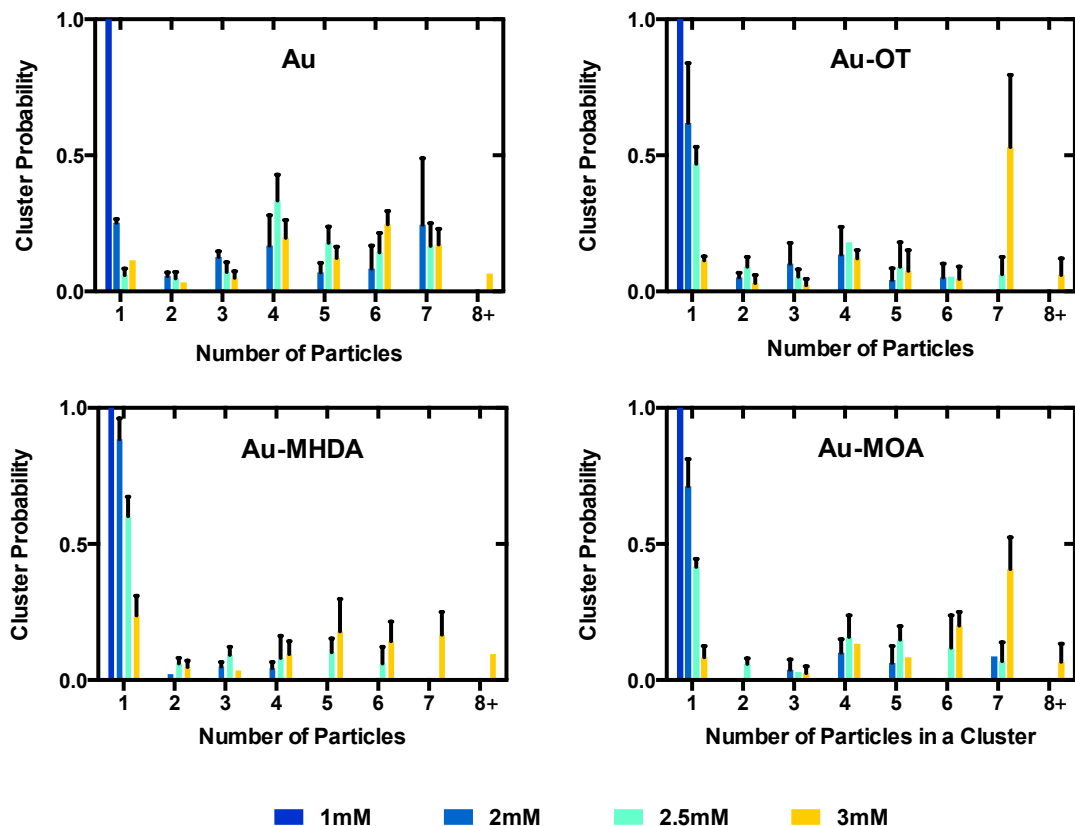


**Figure Appendix A.3 Cluster probability distribution at a fixed hemispheric gold thickness (40 nm) and SAM functionality as a function of NaCl concentration from 1-3 mM.**

This quantity is evaluated for unmodified Janus spheres (Au), Au-OT, Au-MHDA, and Au-MOA modified Janus spheres. All surface conditions resulted in Janus particle self-assembly as the salt concentration is increase. Among the conditions, Au-OT and Au-MOA yielded the highest cluster probabilities of  $n = 7$  at 3 mM.

#### **A.4 Effect of SAM hydrophocity and chain length on cluster size distribution.**

The effect of four different Au hemisphere surface chemistries – no thiol SAM, OT, MOA, and MHDA – on the cluster probability distribution was studied using 40 nm Au-coated Janus spheres at fixed salt concentraions of 2 mM, 2.5 mM, in addition to 3 mM already presented in Figure 2.7. Across all Janus variations, 1 mM experiments produced no clusters and therefore, data

was for that particular salt condition is not plotted in Figure Appendix A.4. For 2 – 3 mM, a thiol functionality comparison under each NaCl concentration is shown in Figure A.4. At 2 mM, Janus spheres without thiol functionality showed the highest amount of  $n = 7$  cluster size. The functionalized Janus spheres remained primarily monomeric in the electrolyte solution at 60 min. At 2.5 mM, the unmodified Janus spheres show the lowest cluster probability for unbounded spheres with the probabilities of the other cluster sizes being similar at various SAM conditions. At 3 mM, there were similar cluster probability distributions for the various SAM conditions.

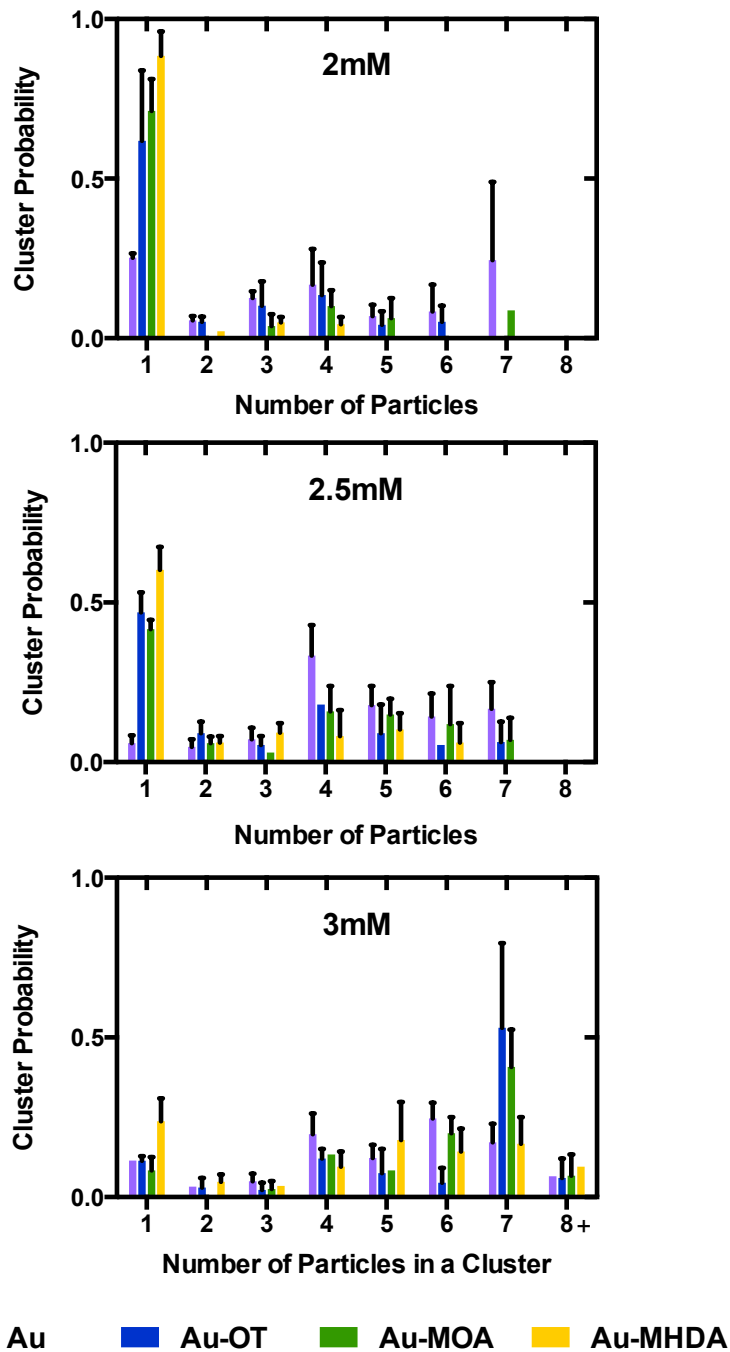


*Figure Appendix A.4 Cluster probability distribution at a fixed hemispheric gold thickness (40 nm) with varied gold functionality.*

This is repeated for fixed NaCl concentrations ranging from 2 – 3 mM. For each salt condition, 2, 2.5 and 3 mM, there is no discernable difference in cluster probability distribution in comparing the surface chemistries as they are influenced by salt.

## A.5 Separation dependent Hamaker coefficient calculations

The van der Waals interaction energy for two flat plates interacting across a medium separated by a distance  $L$ , is given by (ref 24 in Section 2.7)

$$Energy = \frac{-A(L)}{12\rho L^2} \quad [1]$$

The Hamaker coefficient,  $A$ , can be approximated using (ref. 25 in Section 2.7)

$$A = \frac{3kT}{2} \sum_{n=0}^{\infty} \frac{1}{j^3} \frac{e_1(iZ_n) - e_2(iZ_n)}{e_1(iZ_n) + e_2(iZ_n)} \quad [2]$$

where  $k$  is Boltzmann's constant,  $T$  is the temperature, and  $\epsilon_i(i\xi_n)$  is a function of frequency with  $\xi_n = (2\pi kT/\hbar)n$ . The  $n = 0$  term is multiplied by  $1/2$ . The spectral parameters to use in  $\epsilon_i(i\xi_n)$  for polystyrene, gold, and water were also taken from ref. 25 in Section 2.7. In treating the geometry as a flat plate for a short-range approximation of the van der Waals attraction of the pure PS-water-PS and pure Au-water-Au limits, Eq. 1 is used. The interaction energy between multilayered systems is described elsewhere (ref. 23 in Section 2.7) and applied here to Au-coated PS surfaces:

$$\begin{aligned} Energy_{coated\ PS} &= \frac{A_{gwg}}{12\rho L^2} + 2 \frac{A_{pg/gw}}{12\rho (l_g + L)^2} + \frac{A_{pgp}}{12\rho (2l_g + L)^2} \\ &= \frac{A_{gwg}}{12\rho L^2} \left( 1 + 2 \frac{A_{pg/gw} / A_{gwg}}{(l_g / L + 1)^2} + \frac{A_{pgp} / A_{gwg}}{(2l_g / L + 1)^2} \right) \end{aligned} \quad [3]$$

The thickness of the gold layer,  $l_g$ , is varied from 5 – 100 nm. Coefficients for interactions between  $A_{pwp}$  – PS/water interfaces,  $A_{gwg}$  – Au/water interfaces,  $A_{pg/gw}$  – PS/Au interface and Au/water interface, and  $A_{pgp}$  – PS/Au interfaces are given in Table Appendix A.2. For example:

$$A_{pg/gw} = \frac{3kT}{2} \sum_{n=0}^{\infty} \sum_{j=1}^{\infty} \frac{1}{j^3} \frac{\epsilon_p - \epsilon_g}{\epsilon_p + \epsilon_g} \frac{\epsilon_g - \epsilon_w}{\epsilon_g + \epsilon_w} = -5.90 \times 10^{-20} \text{ J}$$

**Table Appendix A.2** Calculated Hamaker coefficients for interfaces included in PS/Au interactions.

$A_{pwp}$	$A_{gwg}$	$A_{pg/gw}$	$A_{pgp}$
$1.38 \times 10^{-20} \text{ J}$	$8.76 \times 10^{-20} \text{ J}$	$-5.90 \times 10^{-20} \text{ J}$	$4.75 \times 10^{-20} \text{ J}$

### A.6 Effective surface coverage using physical vapor deposition

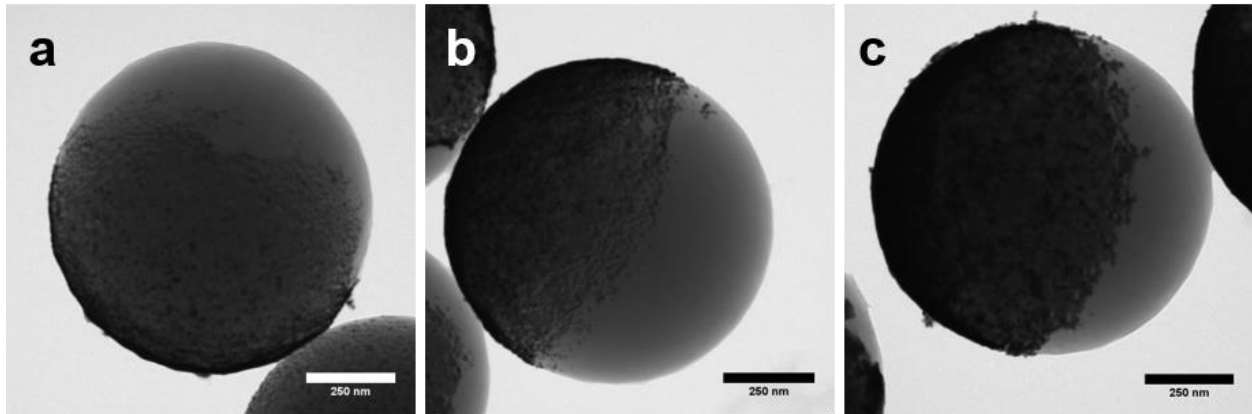


**Figure A.5** Metallic coverage with varied gold thickness.

TEM images of 1 μm PS spheres coated with gold using physical vapor deposition. The gold layer thicknesses are (a) 10nm, (b) 20nm, and (c) 40nm.

TEM images confirm the even coverage of gold using PVD for even the thinnest 10nm layer.